Geochemistry, Geophysics, Geosystems

RESEARCH ARTICLE
10.1029/2023GC011255

Key Points:

- Alongside geology, topography, and hydroclimate, tectonics is the biggest factor for crack generation during the 14 August 2021, M_w 7.2 Haiti earthquake
- Thrust and sinistral strike-slip cracks partition similarly to the earthquake slip pattern and to the oblique-convergence margin

Supporting Information:

Supporting Information may be found in the online version of this article.

Correspondence to:

N. Saint Fleur,
newdeskarl@gmail.com

Citation:

Saint Fleur, N., Dessable, J. E., Saint-Preux, G., Calais, É., Feuillet, N., Boisson, D., et al. (2024). Tectonic, topographic, geologic, and hydroclimatic influence on crack formation during the 2021 Haiti earthquake. *Geochemistry, Geophysics, Geosystems*, *25*, e2023GC011255. https://doi.org/10.1029/2023GC011255

Received 27 SEP 2023
Accepted 28 JUN 2024

Tectonic, Topographic, Geologic, and Hydroclimatic Influence on Crack Formation During the 2021 Haiti Earthquake

Newdeskarl Saint Fleur[1,2], Joseph E. Dessable[2], Germain Saint-Preux[2], Éric Calais[3], Nathalie Feuillet[1], Dominique Boisson[2], Jean-Bernard de Chabalier[1], and Yann Klinger[1]

[1]Université de Paris Cité, Institut de Physique du Globe de Paris, CNRS, Paris, France, [2]Université d'Etat d'Haïti, Faculté des Sciences, LMI CARIBACT, URGéo, Port-au-Prince, Haïti, [3]Département de Géosciences, École Normale Supérieure, Université PSL, Paris, France

Abstract The 14 August 2021 Haiti earthquake mainly portrayed reverse motion to the east near L'Asile town and left-lateral strike-slip motion to the west near Camp-Perrin town. To map the rupture and infer its segmentation, we conducted the first post-seismic field reconnaissance along the left-lateral strike-slip Enriquillo fault from L'Asile to Macaya mountain. We identified 98 linear, minor cracks that are not representative of primary fault surface rupture. Analyzing the topographic slope distribution, we detected that the cracks were often located in areas that are prone to topographic instability. About 60% of the cracks are located in Quaternary alluvium and Middle-Miocene continental marls, indicating a preference for soft sediments. The rivers also have an impact, as crack lengths and openings negatively correlate with their distance to neighboring rivers. In addition, the earthquake occurred in a rainy region with up to 2,479.34 mm of rainfall in 2021, increasing soil instability. Above all, we found a contrast and asymmetry between the eastern and the western parts of the rupture. By dividing the 60-km long rupture into two equal parts, we observed 57 cracks to the west against 41 to the east. The longest and the widest cracks are to the west. Analyzing their orientation, the cracks mainly oriented as left-lateral strike-slip faults to the west and mainly thrusts to the east. This configuration appears to be influenced by the slip pattern of the 2021 Haiti earthquake and consistent with the regional stress field.

1. Introduction

The 14 August 2021, M_w 7.2 Haiti earthquake occurred along the southern peninsula only 11 years after the 12 January 2010, M_w 7.0 devastating earthquake (e.g., Saint Fleur et al., 2015). Even though it released 40% more energy than the 2010 event (Calais et al., 2022), the 2021 earthquake caused 99% fewer casualties. The reason is clearly the fact that the 2010 event occurred near the densely populated city of Port-au-Prince (Figure 1). The ~2,250 deaths from the 2021 event could have been less if, in this hazardous country, disaster preparedness had had a better place in public policy (Benjamin et al., 2011; Cabas et al., 2023). Indeed, the earthquake encountered poor construction and non-application of building codes. Some people were also killed by the earthquake-induced landslides, which were exacerbated by the hurricane Grace occurred only 2 days after the mainshock (Cabas et al., 2023; Giardina et al., 2023; Havenith et al., 2022). Some landslide and rockfall debris caused road blockages, complicating humanitarian assistance amid the COVID-19 pandemic and gang violence.

The 14 August 2021 Haiti earthquake ruptured about 60-km long section along the Enriquillo-Plantain Garden Fault (EPGF) zone between L'Asile to the east and Macaya mountain to the west (e.g., Calais et al., 2022; Figure 2a). The 2021 event was an oblique rupture with dominantly reverse motion to the east near the epicenter and almost pure strike-slip motion to the west (e.g., Calais et al., 2022; Douilly et al., 2023; Maurer et al., 2022; Okuwaki & Fan, 2022). The mainshock and the aftershock epicenters were located to the north of the EPGF surface trace. During the first two months after the mainshock, that is, until November 2021, the aftershocks formed two clusters, an eastern one near L'Asile village and a western one near Camp-Perrin village. Although the eastern cluster portrayed mainly reverse focal mechanism, no significant coastal uplift was observed on the InSAR data (Maurer et al., 2022), consistent with field observation (Saint Fleur et al., 2021). Then, from January–March 2022, a new seismic sequence of magnitude up to 5.3 formed a third cluster near Miragoâne, to the east of the 14 August 2021 earthquake epicenter (Paul et al., 2023).

10.1029/2023GC011255

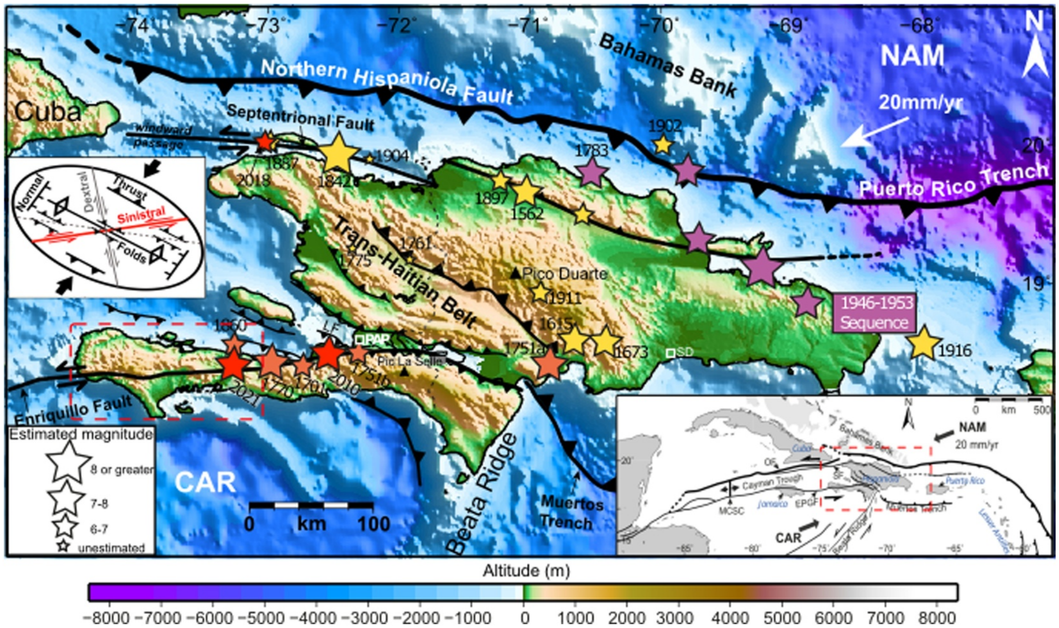

Figure 1. Tectonic setting and historical seismicity of Hispaniola. The oblique convergence of 20 mm/yr between the North American plate and the Caribbean plate is partitioned into (1) two main strike-slip faults: the Septentrional Fault to the north and the Enriquillo Fault to the south; and (2) numerous folds and thrusts forming the Trans-Haitian Belt in between the two strike-slip faults. The yellow and purple stars are from the NOAA database; the orange stars are from Bakun et al. (2012). The red stars highlight recent earthquakes. PAP: Port-au-Prince; SD: Santo Domingo; LF: Lamentin Fault. The red dotted rectangle locates Figure 2a. Central—left inset: simplified strain ellipse in Haiti. Bottom—right inset: regional tectonic setting in the northern Caribbean and location of the main map.

Based on seismological and geodetic data, Calais et al. (2022) proposed that 55% of the rupture initiated on a 60°-north-dipping EPGF as a combination of reverse and strike-slip motion. To the west, 45% of the rupture would be mostly strike-slip on a 71°-north-dipping Ravine du Sud Fault (RSF). Another model using the EPGF as a causative fault imposed a dip of 51°N for that fault to fit the InSAR data to the east (Maurer et al., 2022). This relatively low-dipping EPGF is incompatible with the distribution of the relocated hypocenters (Douilly et al., 2023). In an "unruptured-EPGF" dynamic model, Okuwaki and Fan (2022) suggested that the rupture initiated on an E-W-striking, 63°N-dipping blind thrust and then jumped onto a strike-slip fault propagating westward from the epicenter. That unmapped strike-slip fault would be oriented at a ∼223° azimuth, differing from the major trend of the EPGF (Okuwaki & Fan, 2022). Overall, the slip models proposed so far converge to a pattern in which: (a) reverse motion is dominant to the east along with—albeit less significant—left-lateral strike-slip motion that may involve the EPGF itself as an oblique structure or a combination of a secondary thrust along with the EPGF; and (b) almost purely strike-slip motion prevails to the west.

Given the magnitude (M_w 7.2) of the event and the numerous ground failures reported (Cabas et al., 2023), the 2021 earthquake was first expected to be accompanied by significant fault surface breaks. However, using different geodetic data sets (InSAR), independent studies showed that the rupture only reached the surface along a 5-km-long section within its western part (Calais et al., 2022; Maurer et al., 2022; Raimbault et al., 2023; Wen et al., 2023; Whitworth et al., 2022). With phase gradient analysis on InSAR data, Yin et al. (2023) managed to detect cracks with centimeter-scale horizontal offsets. But, those cracks mainly correspond to post-seismic slip to the east of the rupture area, from L'Asile to Miragoâne.

Besides the 7,091 landslides mapped by Havenith et al. (2022), numerous linear cracks have also been reported all along the rupture area (Saint Fleur et al., 2021; Saint Fleur, Klinger, et al., 2023). In this paper, we analyze and explain the formation of those cracks through different factors: topography, geology, and hydroclimate. We show that, even though the formation of the cracks was influenced by the latter factors, their orientation was controlled by the deformation field and the slip pattern of the 14 August 2021 Haiti earthquake.

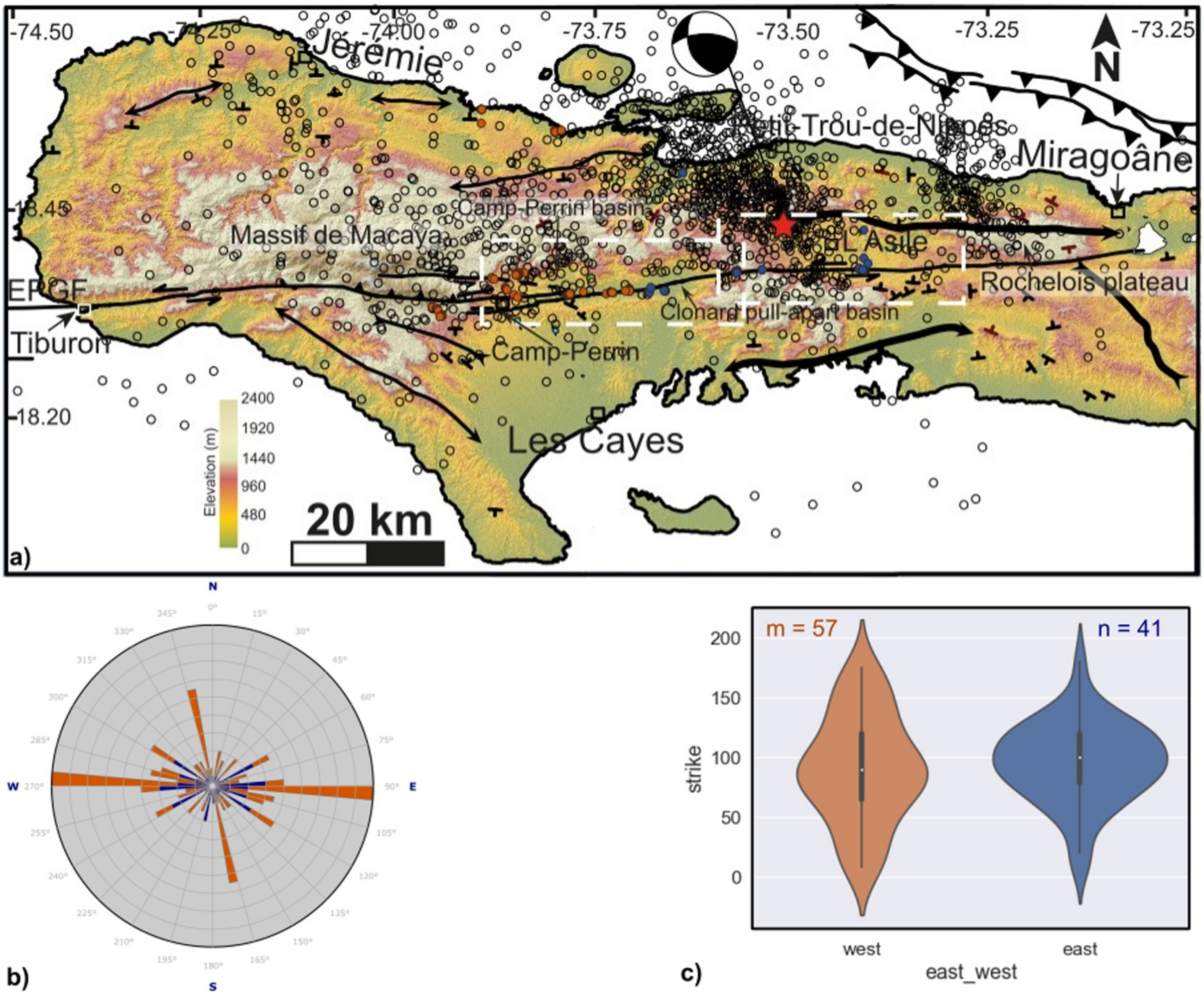

Figure 2. (a) Tectonic map (Saint Fleur et al., 2020) and spatial distribution of coseismic cracks generated during the 14 August 2021 Haiti earthquake. Black dip signs are from the 1:250,000-scale geological map of Haiti (Momplaisir & Boisson, 1988) and the brown ones are inferred from Google Earth. Note major anticlines (black lines with arrows), synclines (black lines with reversed arrows), thrusts (black lines with triangles), and the Enriquillo-Plantain Garden Fault. The 14 August 2021 earthquake epicenter (red star) as well as its focal mechanism are shown. The black empty circles are aftershocks taken from 14 August 2021 to 13 August 2022 for magnitudes greater than 2 from the National Earthquake Information Center catalog. The blue and orange circles represent crack locations to the east and to the west, respectively, according to our separation criterion (see text for details). The eastern and the western white dotted rectangles are the locations of Figures 5a and 7a, respectively. Topographic data: ASTER (pixel: 30 m). (b) Rose diagram showing the general orientation of the cracks. They are mainly E-W and NW-SE. Blue for eastern cracks and orange for western ones. (c) Violin plot showing the density of crack orientation in the eastern and the western parts of the rupture. The number of observations to the east (n) and to the west (m) is annotated.

2. Tectonic Background

The oblique convergence of 20 mm/yr (DeMets et al., 2010) between Caribbean and North American plates (NAMs) induces a transpressional context in Hispaniola, the island shared between Haiti and the Dominican Republic (Figure 1). This transpression is partitioned into shortening and strike-slip (Mann et al., 2002). The strike-slip component is mainly accommodated by two major left-lateral strike-slip faults: the Septentrional Fault to the north and the Enriquillo-Plantain Garden Fault (EPGF) to the south. The 1100-km-long Enriquillo fault crosses the southern peninsula of Haiti in a N85°E direction where its total offset is estimated to 40 ± 10 km (Saint Fleur et al., 2020). From geomorphic analysis and recent GPS data, the best slip-rate estimates of the EPGF vary from 4 to 6 mm/yr (e.g., Calais et al., 2016; Saint Fleur et al., 2020).

The shortening component is mainly accommodated by a series of subparallel folded structures oriented NW-SE referred to "Trans-Haitian Belt" located in the center of the island (Figure 1, Pubellier et al., 1991). Those Miocene anticlines are separated by ramp valleys and continue to the south (Massif de la Selle, Massif de la

Hotte). The anticlines are characterized by high mountains such as pic La Selle (2,680 m), the highest peak in Haiti, and the pico Duarte (3,100 m), the highest peak in the Dominican Republic and the Caribbean. Those Miocene anticlines seem to actively propagate because young (Quaternary) folds are found at their fronts in the ramp valleys. This is the case of numerous young folds and thrusts mapped in the Cul-de-Sac-Enriquillo plain using high-resolution imagery and field observation (Saint Fleur et al., 2019). They are WNW-ESE-striking. One of them (Lamentin) lies in the western suburbs of Port-au-Prince, continues offshore in the bay of Port-au-Prince and has been proposed to have contributed to the oblique rupture of the 12 January 2010 Haiti earthquake (Saint Fleur et al., 2015). The activities of those young folds and thrusts and their geometry were also highlighted in seismological data (Possee et al., 2019; Rodriguez et al., 2018). The recent high-resolution offshore seismic data suggest that the young folds and thrusts system borders the southern peninsula to the north (Calais et al., 2023).

Faults in southern Haiti are responsible for several historical earthquakes (Figure 1). The first reported was the one of 9 November 1701 that caused damage in Port-au-Prince, Petit-Goâve, and Léogâne (Moreau de Saint-Méry, 1798). In 1751, two devastating earthquakes occurred in southern Hispaniola in a 1-month interval and destroyed three-quarters of the buildings in Port-au-Prince. The biggest historical earthquake in southern Haiti occurred on 3 June 1770 (Bakun et al., 2012). Several cities of which Port-au-Prince and Les Cayes were destroyed or severely damaged. Most of the earthquakes in the eighteenth and nineteenth centuries in southern Haiti are generally attributed to the Enriquillo fault, although the tsunamigenic events of 18 October 1751 and 8 April 1860 (Figure 1) may have resulted from rupture at sea, probably by submarine thrust faults (Bakun et al., 2012; Martin & Hough, 2022). During the twentieth century, a relative quiescence was observed until the 12 January 2010 earthquake that was assumed to be the beginning of a new sequence (Saint Fleur et al., 2020). Then, 11 years later, the 14 August 2021 event may be the confirmation of the resumption of the seismic activity in southern Haiti.

3. Data and Methods

3.1. Field Reconnaissance and Data Collection

A few days after the 2021 event, we conducted the first post-seismic field reconnaissance along the left-lateral Enriquillo-Plantain Garden Fault (EPGF) zone from L'Asile town to Macaya mountain (Figure 2). Using our detailed fault map (Saint Fleur et al., 2020), we identified inter alia numerous fresh cracks, landslides, and rockfalls along that fault zone. A reconnaissance along the northern coast of the southern peninsula was also carried out but no clear coastal uplift was identified; this is consistent with the InSAR data (e.g., Maurer et al., 2022). For this reason, we discarded the coastal observations in our analysis. The landslides have been described and mapped by Havenith et al. (2022). Here, we only consider features that may be related to fault surface rupture for analysis (Figure 2a). 98 linear cracks were identified and located with handheld Global Positioning System (GPS) devices. We measured their lengths, openings, strikes, and where it was possible, horizontal and vertical offsets (Table S1 in Supporting Information S1). Then, we added other parameters such as the geological units that underlie the cracks.

3.1.1. Data Processing

We used Pandas, NumPy, and Matplotlib libraries in Python for data processing. We first managed to detect any outliers that could be present due to a typo. We checked the normality by plotting the histograms and the boxplots of the variables (Figures S1 and S2 in Supporting Information S1) as well as by the Kolmogorov-Smirnov test with SciPy (Virtanen et al., 2020). The detected outliers are rather apparent as they reflect marginal data. For example, the apparent outliers in the latitude position of the cracks are due to a few cracks that are located along the northern coast of the southern peninsula (Figure 2a, Figure S2 in Supporting Information S1). The bulk of the observations align along the EPGF zone. As no wrong value was detected for any of the variables, for the rest of the paper an apparent outlier is referred to "exceptional value" or simply "exception." However, some missing values in the variables have to be pointed out. For example, the variable "strike" has 14% missing values, and the variable "opening" 31%. Note that there were no missing values in latitude and longitude. Variables with more than 60% of missing values, such as dips and vertical offsets, were discarded. The remaining missing values were filled using the KNNImputer algorithm (Troyanskaya et al., 2001) from the Scikit-Learn library (Pedregosa et al., 2011). For that, three nearest neighbors were considered and weighted by their distance to the point to be

10.1029/2023GC011255

filled (query point). Closer neighbors of a query point have more influence than farther ones (Troyanskaya et al., 2001).

As the mechanism of the 2021 earthquake is different from east to west (Calais et al., 2022; Douilly et al., 2023; Raimbault et al., 2023), we studied the behavior of the cracks relative to their location. Thus, at the longitude −73.692510°, we divided the 60-km-long rupture into two equal parts: east and west. We identified 41 individual cracks to the east and 57 to the west (Figures 2b and 2c).

The transpressional context induced by the N70°-striking convergence between the Caribbean and NAMs (Benford et al., 2012) favors mainly left-lateral strike-slip oriented roughly E-W and NW-SE reverse faults. But, there are also rare right-lateral faults oriented perpendicularly to the sinistral structures, and likewise, few normal faults oriented perpendicularly to the thrust faults (Mercier de Lépinay et al., 2011; Figure 1, strain ellipse). Finally, following Tchalenko and Ambraseys (1970) and the geometry of the fault system in Haiti, we assimilate each strike value of a crack to a fault type, thus creating a new categorical variable named "strike category" (Table 2 in Supporting Information S1). We then categorized the strike values as follows: (a) dextral, for strike values lower than 10° (angle from north to east) and also for strike values between 160° excluded and 190° excluded; (b) normal, for strike values between 10° included and 70° excluded; (c) sinistral, for strike values between 70° included and 100° excluded; and (d) thrust, for strike values between 100° included and 160° included.

3.2. Topographic Data

The field reconnaissance is complemented with topographic data around the epicentral area including the L'Asile and Clonard basins and the Tiburon valley for geomorphic analysis (Figure 2a). We use a high-resolution LiDAR Digital Elevation Model (DEM) from a data set acquired between 2014 and 2016 (HaitiData & The World Bank, 2021). The spatial resolution is 1.5 m with a 20-cm altimetric accuracy. We use the ENVI software (https://www.l3harrisgeospatial.com/Software-Technology/ENVI) to carry out basic operations on the LiDAR DEM such as splitting, mosaicking and obtaining hill shade images. These data allow a precise fault map in the area of the observed cracks. The LiDAR DEM is also used to precisely map the rivers near the areas of observation.

Then, to analyze the influence of the topography on the cracks, we use the slope of the terrain that underlies the cracks. For a regional view, we generate a slope map from ASTER DEM of 30 m of pixel size (Figure 3a). We also benefit from a slope classification for the southern peninsula from the Centre National de l'Information Géo-Spatiale (CNIGS, Figure S3 in Supporting Information S1). The slope classes were derived from a DEM of the Shutter Radar Topography Mission (SRTM, pixel: 30 m). Then, LiDAR DEM was used to generate a slope map and topographic profiles for topographic analysis down the scale of the crack clusters (Figures 3b–3d). We use the zonal statistics module in QGIS to extract slope data at each individual crack observation (Figure 3, Tables S3 and S4 in Supporting Information S1).

3.3. Hydroclimatic Data

In general, some ground failures observed during earthquakes may be exacerbated by gravity and slope instabilities in addition to the ground motion (Delorme et al., 2020). Other things being equal, the gravity effect is higher for wet soils than for dry ones. Here, we use rainfall data to examine their potential influence on crack generation during an earthquake.

The data set was collected by the Climate Hazards Group InfraRed Precipitation with Stations (CHIRPS). That quasiglobal data set is available with a pixel size of 0.05° or ∼5 km (Funk et al., 2014, 2015). They use global rain gauge data and incorporate satellite information in areas with sparse gauge data. They record precipitation estimates based on infrared Cold Cloud Duration observations. The data set contains rainfall data from 1981 to present. It was possible to obtain the rainfall data for the year of 2021 for the rupture zone to obtain information on the level of rainfall during the year of the earthquake. Thus, we could compare rainfall levels in the areas of observed cracks. The CHIRPS data did not require additional processing on the part of the end user. We use QGIS software (https://qgis.org/) for their visualization, extracting the area of interest and applying a color palette (Figure 4, Figures S4 and S5 in Supporting Information S1). Given the pixel size, only 258 pixels were accounted for our area of interest, from Tiburon to Miragoâne. Profiles of the rainfall data were made using the Geomorphometric analysis module of WhiteboxTools software (Lindsay, 2014).

10.1029/2023GC011255

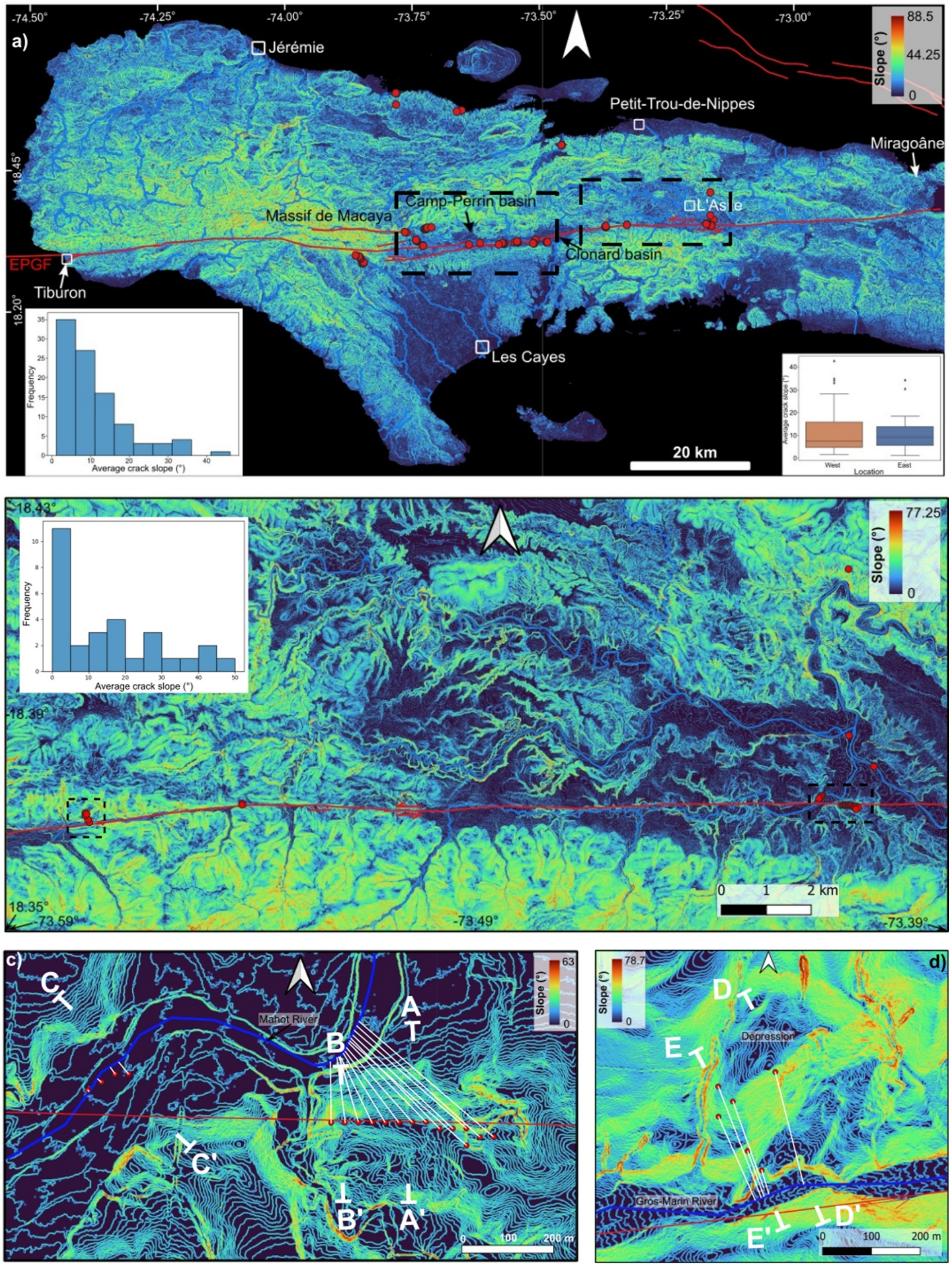

Figure 3. (a) Slope map in southern Haiti derived from ASTER Digital Elevation Model (DEM). Bottom-left inset: histogram of average slope underlying the cracks. Bottom-right inset: boxplot showing the distribution of average crack slope to the east and to the west. Eastern and western, black dotted rectangles are the locations of (b) and Figure 10a, respectively. (b) Slope map derived from LiDAR DEM centered on the L'Asile basin. The same pattern is found at that scale; the cracks (red circles) are located in areas of slope breaks of tens of degrees. Inset: histogram of the average slope of crack in L'Asile. Eastern and western, black dotted rectangles are locations of (c) and (d), respectively. (c) Slope map near Mahot river. The cracks are located on the slope break created by the EPGF scarp. The thin, white lines are schematic distances of each crack with respect to the main neighboring river (Mahot). AA'-CC' are the location of cross-sections of in Figure 9. (d) Slope map near the Gros-Marin River. The cracks are located on a slope break formed by the edge of a topographic depression. The thin, white lines are schematic distances of each crack with respect to the main neighboring river (Gros-Marin). DD' and EE' are locations of cross-sections in Figure 9.

10.1029/2023GC011255

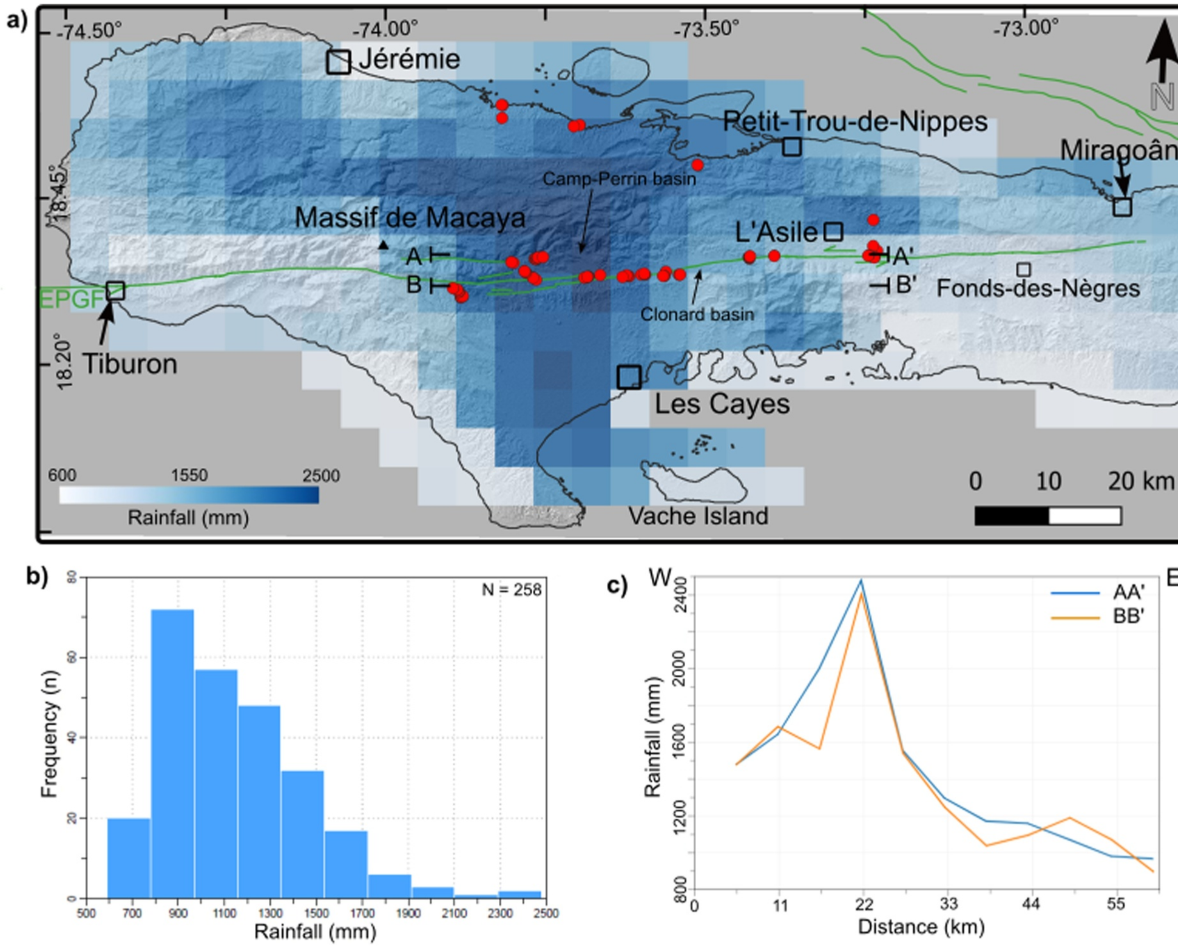

Figure 4. Rainfall in southern Haiti for the year 2021. (a) Rainfall distribution raster (pixel: 5 km) overlain on a hillshade ASTER Digital Elevation Model (pixel: 30 m) showing that the region of the earthquake is rainy with peak rainfall on Macaya mountain and Camp-Perrin basin. AA' and BB' locate profiles in (c). (b) Histogram of the rainfall values. (c) Profiles evidencing that the cracks are located in areas of high rainfall values with the highest to the west. Rainfall data from the Climate Hazards Group InfraRed Precipitation with Stations (CHIRPS).

In addition to precipitation, we analyzed the distance between each individual crack and the nearest river. We consider the major rivers as they are more prone to influence crack formation. We measured the approximate distance on georeferenced maps (Figures 3c and 3d) after fieldwork. If a crack is exactly situated in a dry riverbed, the distance to that river is zero. For three cracks along the northern coast of the peninsula where there are no nearby rivers, the distance was measured with respect to the sea.

4. Results

4.1. Active Deformation and Coseismic Cracks in L'Asile Basin

The L'Asile basin is located between the Rochelois plateau to the east and the Clonard basin to the west. It has Middle-Miocene continental units which lie unconformably upon the older Late-Cretaceous folded units (Bien-aimé Momplaisir, 1986). The sedimentary deposit is further thickened by modern alluvial sediments as the basin is crossed by numerous rivers (Figure 5a). East of the basin, a linear E-W-striking slope break is continuous over 10 km. The linearity shows that the slope break is not a riser of the Serpente river. The lowest topography, as low as 20 m high, is encountered in the center of the basin that is frequently sedimented by the rivers. Thus, the EPGF is not clear in the center of the basin. One can infer its trace by joining its alignment from east to west where it crosscuts the Late-Cretaceous limestone. At this place, the fault corresponds in part to the Citronnier riverbed, where the course is deflected and controlled by faulting. Along this portion, the direction of the fault veers progressively by 4° clockwise before cutting westward in the middle of the Clonard basin.

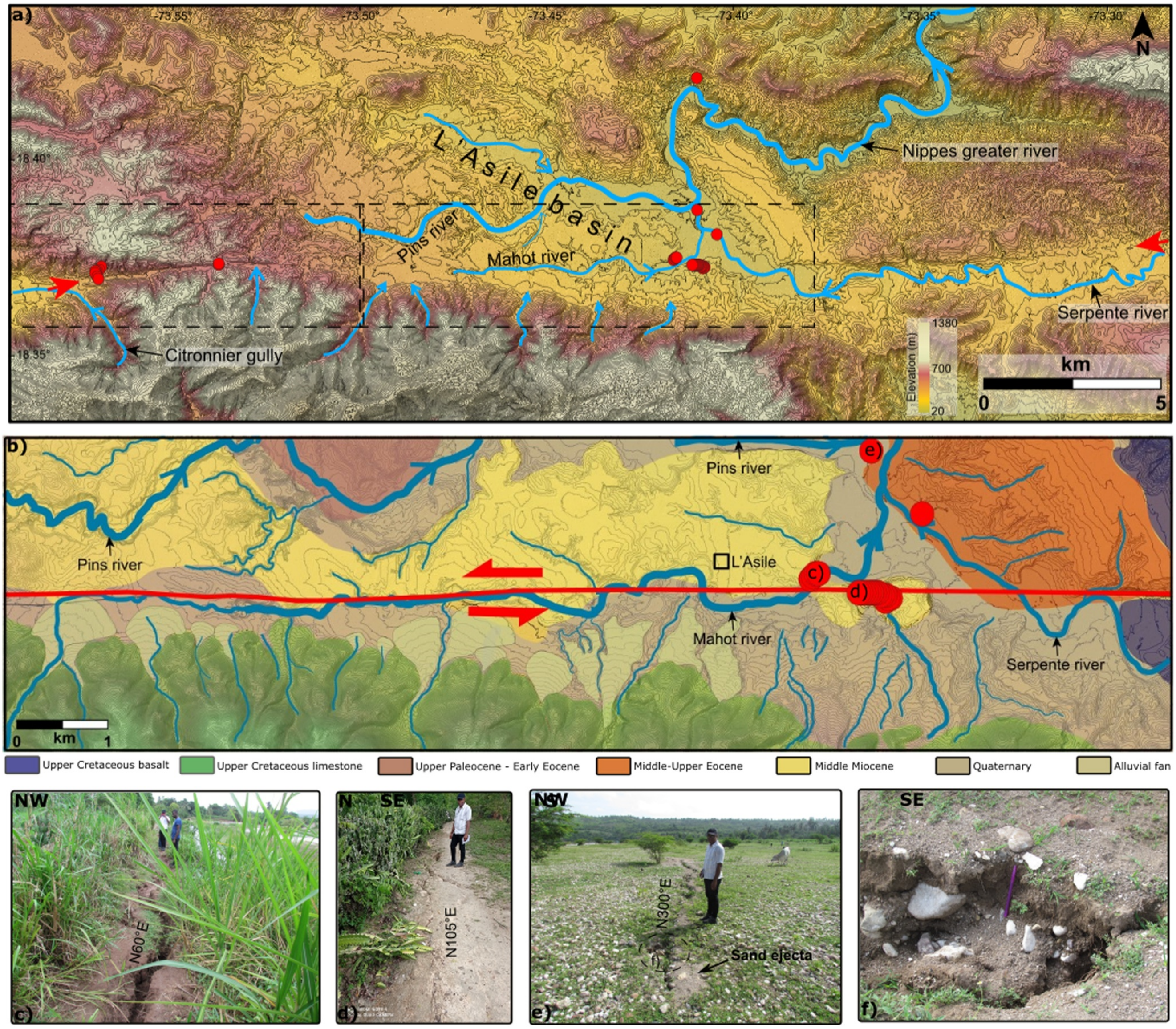

Figure 5. (a) Topographic map of the L'Asile basin. The EPGF surface trace is between the red arrows. Red circles represent crack locations. Contours are at 20-m intervals. Central and western, black dotted rectangles are locations of (b) and Figure 6, respectively. Topographic data: LiDAR (pixel: 1.5 m). (b) Geological map of central L'Asile. Geological contours have been redrawn from Momplaisir and Boisson (1988). LiDAR topographic contours are 5-m intervals. Note the locations of the photographs in (c–e). (c–f) Photos of 2021 coseismic cracks (see text for discussion).

The central L'Asile basin is surrounded by several high mountains corresponding to Cretaceous limestone (green) to the south and to the west, Cretaceous basalt (blue) and Paleocene limestone to the north and to the east (Figure 5b). In the middle are marls of Middle-Miocene age (yellow) and Quaternary soft sediments (gray). The basin is crossed by three main rivers: Pins, Mahot and Serpente. The EPGF controls the course of the Mahot River running parallel to it. During the 2021 post-seismic fieldwork, we started observations in central L'Asile. As the bulk of the observations were carried out along the EPGF surface trace, the cracks were near rivers and often on riverbanks, which make discriminating fault surface rupture from gravity-related ground-failure difficult. On Figure 5c shows an example of a crack that is parallel to the Mahot riverbank. The crack is N60°E-striking, 100-m long and 20-cm wide. At 500-m to the east, we located a series of relatively deep cracks in the marl rock (Figure 5d). Those are 200 m long and 10 cm wide and have orientation varying from N90°E to N300°E. At 1.5 km to the north near the intersection of the 3 rivers (Pins, Mahot, Serpente), a linear crack was seen from which sand came out (Figure 5e). That crack is 100-m long, 20-cm wide and N300°E-striking.

10.1029/2023GC011255

Figure 6. (a) Fault mapping and coseismic cracks in western L'Asile. LiDAR topographic contours are 5-m intervals. Note the locations of the photographs in (b, d). (b) Crack in Nan Tetis. The land dips to the south. (c) Zoom showing apparent vertical offset in (b). The green and white object is a notebook for scale. (d) Crack in Carrefour Suzanne. The land dips to the south. (e) Apparent vertical offset of the Carrefour Suzanne crack.

From central L'Asile, the EPGF continues straight to the west where it is well expressed through the Cretaceous massive limestone (Figure 6a). Along that section are some of the most prominent cracks. In Nan Tetis, we found a 300-m long and N87.5°E-striking crack (Figures 6b and 6c). It topographically stands at least at 100-m higher from the Citronnier gully. At 3.5 km to the east, Carrefour Suzanne is another crack. It is E-W-striking, 20-cm wide and 100-m long (Figure 6d). It has an apparent vertical offset of 50 cm (Figure 6e). However, that vertical offset may be influenced by the south-dip of the bank of the Citronnier gully. Eyewitnesses affirmed that the crack continued without interruption to the west, which the Geotechnical Extreme Events Reconnaissance team confirmed (Cabas et al., 2023). Based on that information, the Carrefour Suzanne and Nan Tetis cracks may be connected.

4.2. Active Deformation and Coseismic Cracks in Clonard and Camp-Perrin Basins

The Clonard basin is a ~24-km spindle-shaped pull-apart along the EPGF (Figure 2a). In the middle of the Clonard basin, the main fault is well-expressed and exhibits a well-preserved ~2-m high scarp in the Quaternary alluvium (Saint Fleur et al., 2020). In this area, the fault controls the course of the Cavaillon River flowing from the basin of Camp-Perrin (Figure 7a). The Camp-Perrin and Clonard basins are connected by the wide Cavaillon riverbed, overall forming a ~30-km long and up-to-5- km wide depression. This depression is filled with Quaternary sediments brought by numerous active rivers which all converge toward this area. The basin of Clonard, in particular, is completely filled with Late Quaternary sediment that is offset by faulting attesting for Late Quaternary activity (Saint Fleur et al., 2020). West of the Clonard Basin, the fault crosscuts several meanders and terraces of the Cavaillon River. Along this section are numerous cracks associated with the 14 August 2021 earthquake. Figure 7b shows a N275°E-striking 50-m long crack cutting a road. The latter is not left-laterally offset by the crack as expected. Along the bank of the Cavaillon River are a series of relatively deep and wide cracks (Figure 7c). They are N110°E and 100-m long. Then, on a terrace of the river are a N85°E-striking and 40-m long crack showing down-throw toward the river (Figures 7d and 7e).

While the cracks in the Clonard basin were not accompanied by lateral offsets, in the Camp-Perrin basin several of such offsets—even apparent—were identified. Indeed, the road of Camp-Perrin showed several horizontal

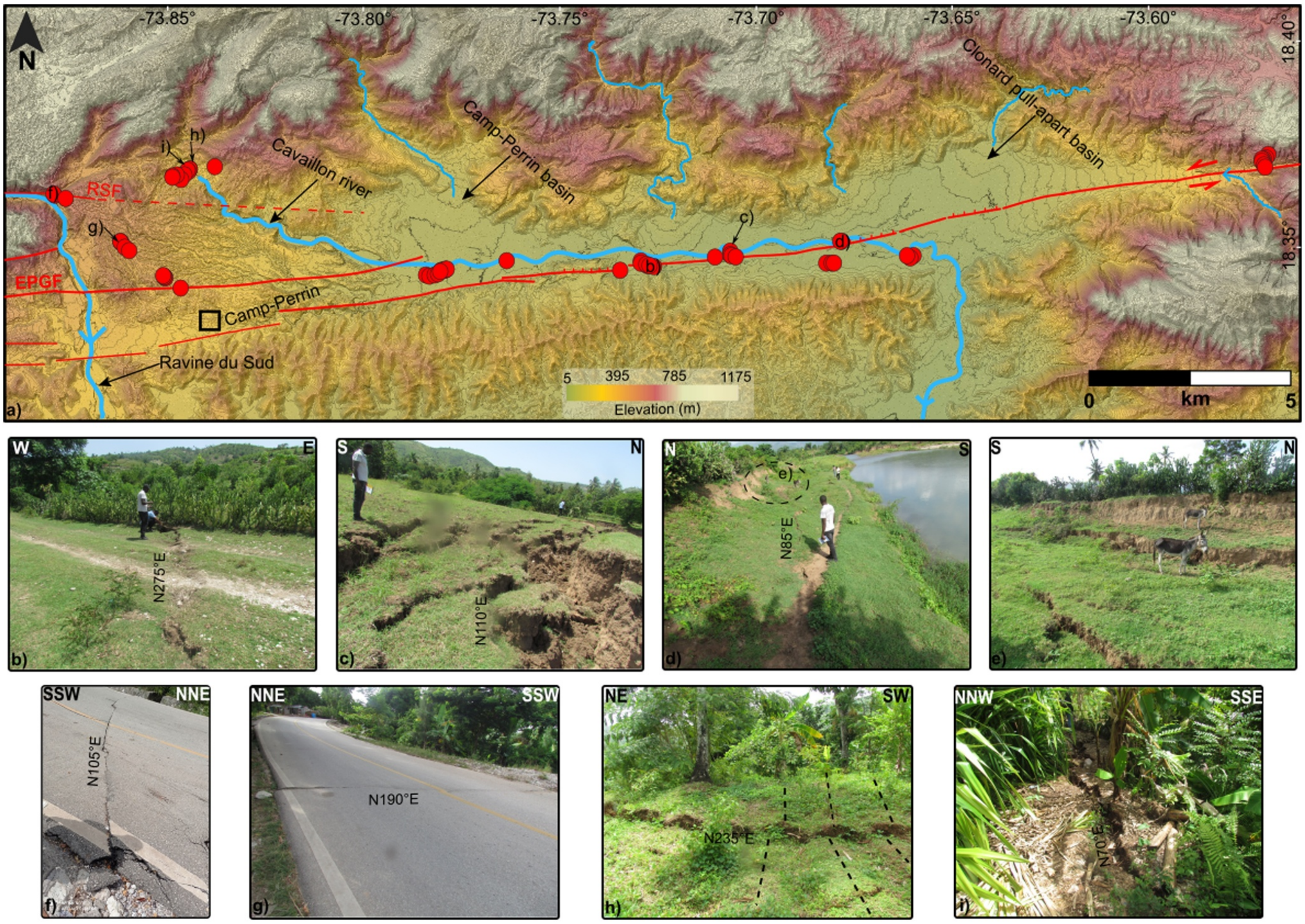

Figure 7. (a) Fault mapping and coseismic cracks in Clonard and Camp-Perrin basins. Contours are 10-m intervals. Note the locations of the photographs in (b–i). (b) Path unoffset by the crack. (c) Multiple large cracks crumbling toward the Cavaillon River. (d) Crack with vertical offset on a terrace of Cavaillon River. (e) Close-up from (d). (f) Crack left-laterally offsetting the road of Camp-Perrin of 10 cm. (g) Right-lateral offset on the road of Camp-Perrin. (h) Apparent right-lateral offset of a farm (see text for discussion). (i) Crack without visible horizontal offset.

offsets. The pavement is left-laterally offset 10 cm (Figure 7f). That crack, located 205 m from the Ravine du Sud River, is N105°E-striking, 7-m long, and 5-cm wide. About 2 km southward, the pavement is again offset but right-laterally by 10 cm (Figure 7g). The crack is 1,415 m from the Ravine du Sud (Figure 7a). It is 7-m, 2-cm wide and N190°E-striking. This kind of crack is not expected, but its orientation is consistent with the regional stress field (Figure 1). On the northern edge of the Camp-Perrin basin is a farm with furrows and ridges that appeared to be right-laterally offset by 50 cm (Figure 7h). The crack is 70 m from the river of Cavaillon. It is 150-m long, 20-cm wide and N235°E-striking. With 15 cm, that crack has one of the most prominent vertical offsets among the observed linear cracks. The opening of 20 cm also makes the crack among the widest. Those characteristics along with the orientation support that the crack may only displace the ground vertically in the manner of a normal fault. In this case, the prementioned right-lateral offset is only apparent. About 200 m to the southwest is a relatively deep crack striking N70°E without any visible horizontal offset (Figure 7i). As far as we could measure under the brushwood, that crack has a length of 200 m and an opening of 20 cm. The distance of that crack to the Cavaillon River is 40 m.

4.3. Overview of Different Forcings of Crack Formation During the 2021 Haiti Earthquake

4.3.1. Geology

Earthquake-induced ground acceleration may create soil instability and thus ground-failure. In this case, the underlying geological units may be prone to failure (Valkaniotis et al., 2014) or control rupture propagation

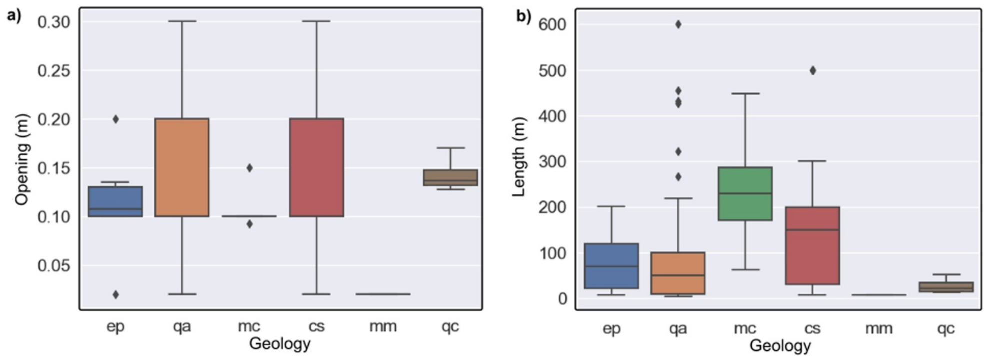

Figure 8. Possible relationship between crack magnitude and the geological units. (a) Boxplots of geological units with respect to crack openings showing that the widest cracks are on Quaternary alluvial sediments (qa) and the Cretaceous limestone (cs). (b) Boxplots showing that cracks on the Quaternary alluvial sediments and on the Middle-Miocene continental marls are the longest. In each box, the black horizontal central line indicates the median value. Black diamond markers indicate exceptional values. The box lower and upper edges correspond to the 25th and 75th percentiles, respectively.

(Vallage et al., 2016). Here, we analyze the spatial distribution of the cracks over the geological units in southern Haiti using a 1:250,000-scale geological map (Momplaisir & Boisson, 1988). Since most of the cracks spread along the EPGF zone, rock characteristics are not decisive for crack formation. However, the geology in southern Haiti seems to influence crack magnitude (Figure 8). Indeed, crack openings and lengths tend to increase in soft sediments. The Quaternary alluvial sediments (qa) have cracks of all possible opening values, from 2 to 30 cm with 10 cm as the median value (Figure 8a). The Late-Cretaceous limestone (cs) also includes the entire opening range with a median at 10 cm. In the Late Paleocene-Early Eocene limestone, the openings of the cracks are between the exceptional values of 2 and 20 cm, but the bulk of the openings in the Paleocene-Early Eocene limestone are between 10 and 13 cm. For the cracks in the Middle Miocene, continental marls (mc), their openings are 10 cm with two exceptions of 9 and 15 cm (Figure 8a). Nonetheless, crack lengths in that marl are among the greatest (Figure 8b). Indeed, while the length values in the whole data set span from 3 to 600 m, 90% of the cracks in the marl are greater than 100-m long and up to 450 m (Figure 8b, Table S2 in Supporting Information S1). Once again, crack lengths vary greatly in Quaternary alluvial deposits from 3 to 600 m, with 25% of the points greater than 100 m. In the Late Cretaceous limestone, the cracks have 50% of their length values between 150 and 500 m. In the Late Paleocene-Early Eocene limestone, the crack lengths are between 7 and 200 m, with 25% greater than 120 m. Finally, only one crack is located on the Middle Miocene limestone, dominantly detrital (mm); it is 7-m long and 2-cm wide. The cracks on the Quaternary coral platform (qc) have openings of 12–17 cm and lengths between 12 and 52 m.

4.3.2. Topography

Topography is also related to crack formation during an earthquake. The L'Asile basin has places as low as 20-m above sea level, but it is surrounded by highlands of up to 1,380 m (Figure 5a). The high-resolution of the LiDAR DEM allows us to observe that the center of the basin is heterogeneous in slopes. There, the cracks are located where the slopes are up to 50° (Figure 3b). Near the Mahot River, an eastern crack cluster is located and aligned on the EPGF scarp as an area of slope contrast (Figure 3c). Indeed, despite the subtle trace of the fault, the latter forms an elongate ridge of which most of slope values are 20°–25° at its top and down to 0° at its base. The fault scarp is more than 5 m high (Figures 3b, 9AA', and 9BB'). The cracks are precisely formed at the base of the scarp. The numerous rivers crossing the basin form significant slope gradients as their banks can reach 60°–70° and their beds can be as low as 0°. The Mahot River has cracks formed between its flat bed and its talus where the slope gradient is the highest (Figure 9CC').

Western L'Asile, the area separating the L'Asile basin from the Clonard basin, comprises highlands up to 935 m high (Figure 6a) and a slope of 40° (Figures 3b and 3d). There, the cracks are located on high-slope riverbanks of narrow tributaries of the Gros-Marin River. Although some cracks are located on riverbanks, some are rather located on the edges of topographic depressions about 200 m from the Gros-Marin riverbed (Figures 9DD' and 9EE'). The depression edges have slopes of 40–50° in contrast to the center where slopes are 10° in average.

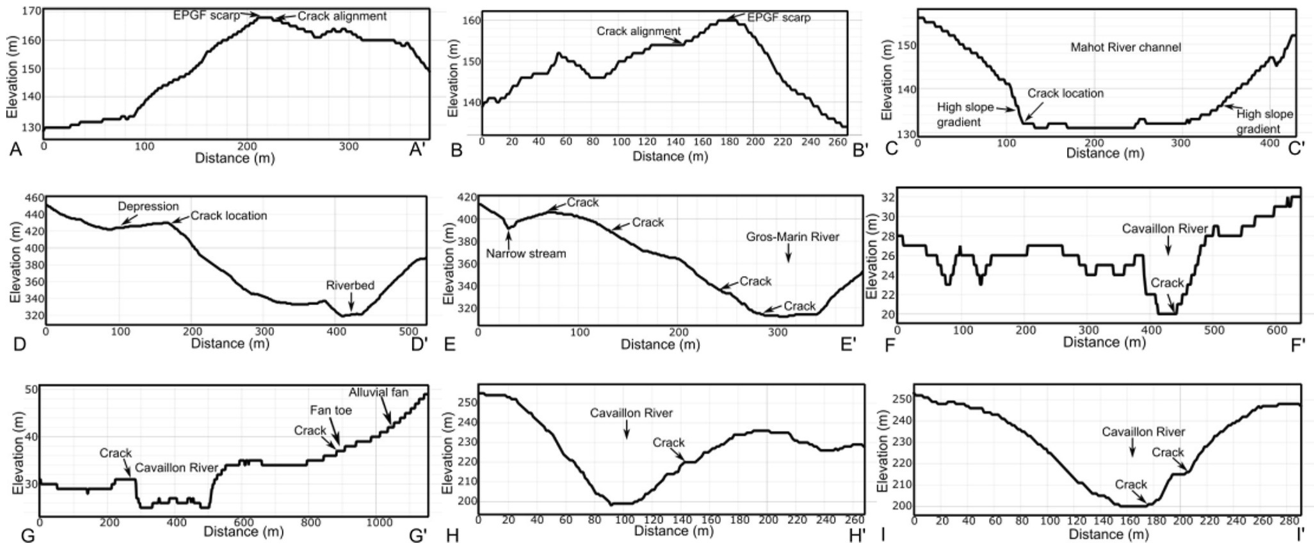

Figure 9. Topographic cross-sections on LiDAR Digital Elevation Model showing crack locations in areas prone to ground instability. Stair-step appearance of the profiles, particularly in FF' and GG', is due to lack of topographic variation in areas like Clonard basin mainly made of alluvial terraces of the Cavaillon River. See location in Figures 3c, 3d, 10b, and 10c.

In the basin of Clonard, crack slopes are 5°–10° (Figures 3a and 10a). Some are located on a flat terrace of the Cavaillon River. In the basin of Camp-Perrin, the topography is more varied than in the basin of Clonard. There, the crack slopes can be as low as 0° and as high as 40°. Like in the L'Asile basin, the basins of Clonard and Camp-Perrin are heterogeneous in slopes (Figure 10a). The highlands, Massif de Macaya, surrounding this depression area have slopes of up to 80°. In the two basins, high slope gradients are formed by the numerous riverbanks and their corresponding riverbeds. High gradients are also observed along fault scarps. A crack cluster is observed in the Clonard basin with a general gentle slope, given the large spacings between areas (apparent lines) of the same slope values (Figures 9FF', 9GG', and 10b). This general gentle slope is disturbed by the steep and elongated Cavaillon riverbank. Many cracks are obviously located on the bank. The slope map also evidenced a series of alluvial fans formed by numerous tributaries of the Cavaillon River. Though subtle, the fan toes form abrupt slope breaks between the fans and flat terraces of the main river (Cavaillon). Some cracks are located on the fan toes (Figure 10b).

Looking at a crack cluster at the northern edge of the Camp-Perrin basin, the cracks are mainly located along the Cavaillon riverbank where slopes reach 70° with respect to the riverbed where slopes are as low as 0% (Figure 10c). Overall, the high-resolution slope maps derived from the LiDAR data show that the cracks are rarely located on flat ground or areas with regular slopes.

4.3.3. Hydroclimate

One of the geomorphic objects creating slope contrasts is the rivers when we consider the significant height difference that may exist between riverbeds and riverbanks. Instability of riverbanks is exacerbated by the geological properties of the bank, lateral erosion and specific hydrodynamic conditions (Darby & Thorne, 1994; Hackney et al., 2020; Mohammed-Ali, 2020; Thorne & Abt, 1993). Even more so, in the presence of strong ground motion during the 2021 Haiti earthquake, the steep riverbanks, mainly made of soft sediments, massively broke down. Along the riverbanks, the cracks often show opening migration toward the riverbeds (Figures 7c–7e), which is inter alia an indication of the gravity influence toward the part of the bank that faces the river.

In addition to the susceptibility of the riverbank to break down during the earthquake, we tested river influence on crack magnitude. We first measured the distance of each crack to the nearest neighboring river. The distances spanned from 0 (cracks in riverbed) to 2,320 m. About 87% of the cracks are located at less than 600 m from a river, ~73% at less than 300 m, ~64% at less than 200 m, and ~44% at less than 100 m (Figure 11, Table S2 in Supporting Information S1). Then, we plotted those distances as a function of the crack openings and lengths,

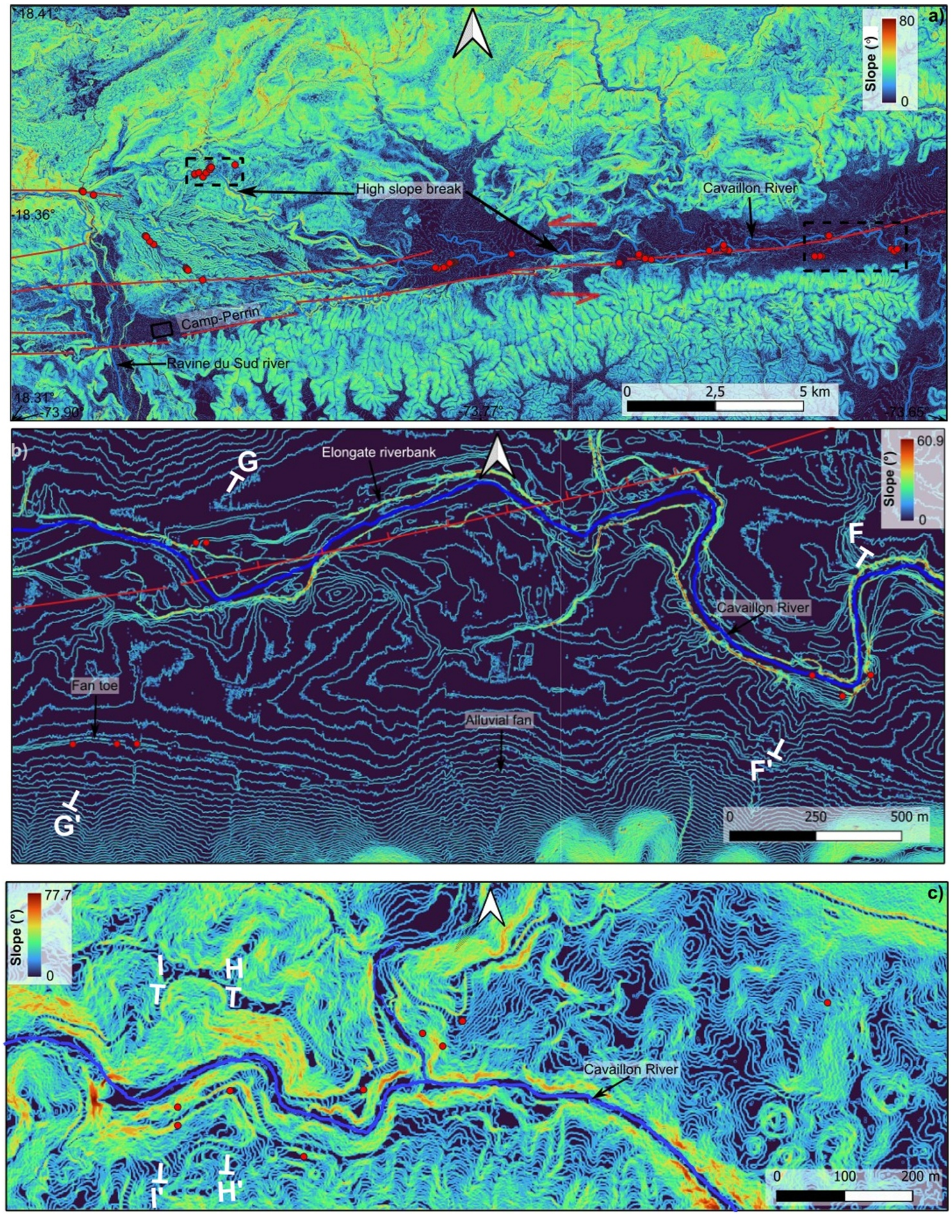

Figure 10. (a) Slope map in Camp-Perrin and Clonard basins. The slopes are up to 80° on the highlands surrounding the basins. Red circles represent crack locations. Circle size is reduced to better match their locations to slope values. Eastern and western, black dotted rectangles are the locations of (b) and (c), respectively. (b) Map showing cracks located on areas of high slope gradients like the Cavaillon riverbank and fan toes. FF' and GG' are cross-section locations in Figure 9. (c) Map showing a crack cluster on the northern edge of the Camp-Perrin basin. The cracks are mostly located on riverbanks. HH' and II' are cross-section locations in Figure 9.

respectively (Figures 11a and 11b). We found that crack openings increased exponentially when the distance to rivers was smaller (Figures 11a and 11c). Crack lengths themselves increased slightly with decreasing distances to rivers.

As a waterlogged soil is sensitive to ground failure, we also analyzed rainfall in southern Haiti during the year of 2021. Figure 4a shows rainfall from 591.59 to 2,479.34 mm with a mean value of 1,143.68 mm. More than 60% of territories around the epicentral area have rainfall greater than 1,000 mm (Figure 4b). The Massif de Macaya culminating at an elevation of 2,360 m along with the basin of Camp-Perrin are the areas with the highest rainfall values. Helped by Hurricane Grace, Macaya Mountain underwent most of the landslides days after the 2021

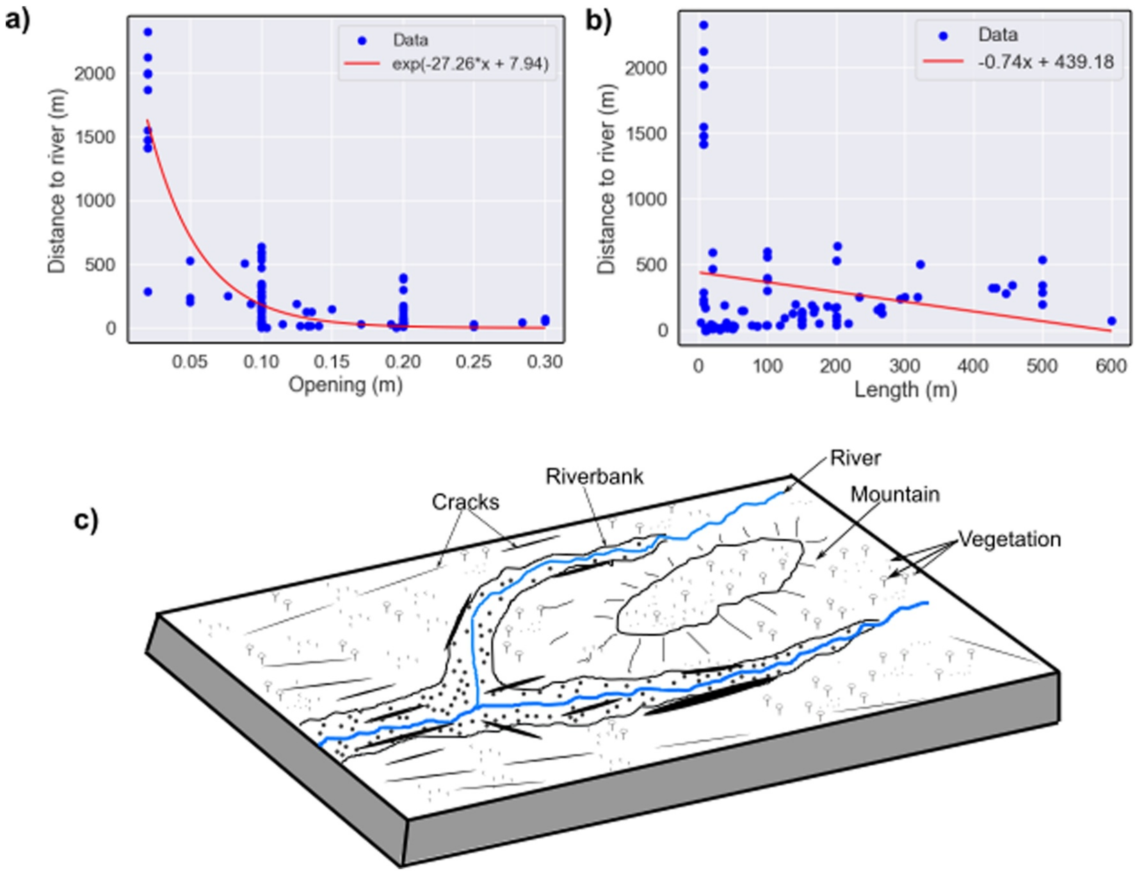

Figure 11. Relationship between crack magnitude and distance to nearest neighboring rivers. (a) Scatterplot of distance of cracks to rivers as a function of their openings. The distances decrease exponentially with the openings. The data was also fitted by discarding the exceptional values greater than 1,600 m for the distances and greater than 0.25 m for the openings. Worse fits were obtained when discarding distances greater than 1,000 m (Figure S6 in Supporting Information S1). The CurveFit module of the SciPy library (Virtanen et al., 2020) was used to fit the data. (b) Distance to river as a function of length. At a distance of 500 m and lower, the distance to the river linearly decreases with crack length. The data was also fitted by discarding the exceptional values greater than 1,600 m for the distances and greater than 300 m for the lengths. Worse fits were obtained when discarding distances greater than 1,000 m (Figure S6 in Supporting Information S1). The Polyfit module of NumPy (Harris et al., 2020) was used to fit the data. (c) Cartoon of the data in (a) and (b) showing the widest and longest cracks near rivers.

mainshock (Havenith et al., 2022). The areas of the lowest rainfall values are to the west (Tiburon valley) and to the east (Fonds-des-Nègres) of the 2021 rupture. Other areas such as the northern coast of Jérémie and Vache island need data of better resolution to confirm their low rainfall level. The whole 2021 rupture zone appears to be captured by a high rainfall level (Figure 4c). More specifically, the cracks in central L'Asile (Figures 5a and 5b) were located in an area where the rainfall level was 967.45 mm, albeit 4 km to the north of that area rainfall was 1,448.22 mm. In western L'Asile, the cracks in Carrefour Suzanne were in an area where rainfall was 1,072.30 mm, whereas in Nan Tetis the rainfall was 1,160.17 mm. In the basin of Clonard, cracks are in areas where rainfall is 1,247.43, 1,539.53, and 2,403.71 mm (Figure 4c). The cracks in the basin of Camp-Perrin encounter rainfall from 1,565.11 to 2,002.21 mm. The 2021 rainfall level is not that surprising, as the region of the earthquake is basically rainy, considering the high rainfall level over the last 10 years, that is 2012–2021 (Figure S4 in Supporting Information S1).

4.3.4. Tectonics

Although several environmental forcings may explain crack formation, it is worth mentioning that this kind of surface deformation mainly occurred along the Enriquillo fault zone. At the same time, landslides, rockfalls, mass wasting occurred all over the mountainous region, and soil liquefaction occurred in the plain of Les Cayes (Cabas et al., 2023). Thus, it is not a coincidence that the linear ground failures, that is, the cracks occurred preferentially along the main fault zone. In the frame of the regional geodynamics, some fault families such as sinistral strike-

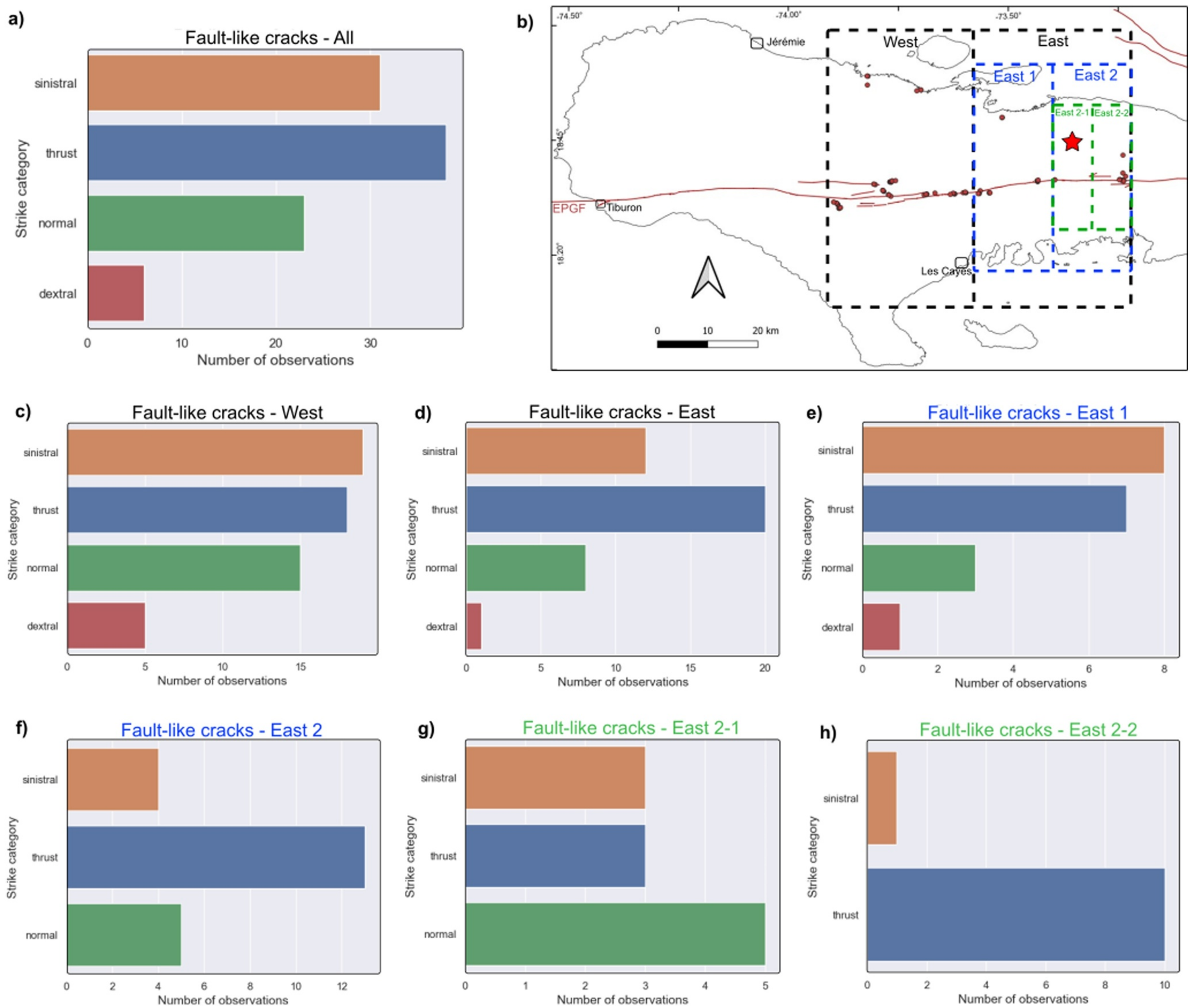

Figure 12. (a) Barplot of the crack strike category for all the cracks showing more thrust fault-like cracks than sinistral strike-slip ones. (b) Map of southern Haiti shows the division, the subdivision, and the sub-subdivision of the rupture area. The box names and colors match their graphs in (c–h). (c) Fault-like cracks to the west are basically sinistral and second thrust. (d) To the east the fault-like cracks are first thrust and then sinistral. (e) Subdivision East 1: first, sinistral; second, thrusts. (f) Subdivision East 2: first, thrust; second, sinistral. (g) Sub-subdivision East 2-1: same number of cracks of both sinistral and thrust. (h) Sub-subdivision East 2-2: 10 thrusts against one sinistral (see text for discussion).

slip and thrust faults are primarily expected (Figure 1). From that, we considered the cracks as faults and compared their orientation with that of different fault types that are likely to be encountered in southern Haiti as defined in Section 3.1.1. Overall, we found that 31.6% of the cracks were oriented as sinistral strike-slip faults, 38.7% as thrust, 23.4% as normal, and 6.1% as dextral (Figure 12a). Sinistral and thrust, with an overall strike interval of N70°–160°E (Figures 2c and 2d), represent more than 70% of the cracks, reflecting main fault types in southern Haiti (Saint Fleur et al., 2019, 2020).

We then analyzed the crack orientation and fault-like categories in the western and eastern parts of the rupture separately (Figure 12b). For the 30-km western part, of the 57 cracks, 19 are oriented as sinistral, 18 as thrust, 15 as normal, and 5 as dextral (Figure 12c). There are very slightly more sinistral fault-like cracks than thrust ones, but together they represent ~65% of the western cracks. However, in the eastern part, there are more thrust than sinistral fault-like cracks (Figure 12d). Indeed, over 41 cracks, there are 20 thrust fault-like cracks, 12 sinistral, 8 normal, and 1 dextral. Thus, 78% are either thrust or sinistral.

10.1029/2023GC011255

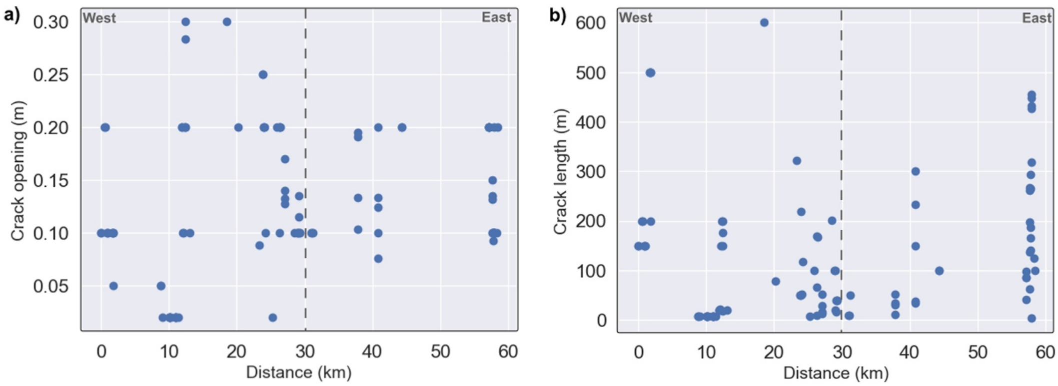

Figure 13. Plots showing the longest (a) and the widest (b) cracks to the west of the 2021 seismic rupture. The dotted line divides the eastern and the western parts of the rupture.

At the median longitude (−73.4775°) of the 30-km long eastern part, we subdivided it into two equal subparts: east 1 to the "west" and east 2 to the "east" (Figure 12b). In east 1 subpart, 8 over 19 cracks within the subpart are sinistral strike-slip fault-like cracks, 7 are thrust, 3 is normal, and 1 is dextral (Figure 12e). With 42%, the sinistral cracks slightly prevail over the thrust cracks (36.8%) in this east 1 part. However, in the east 2 part, the thrust fault-like cracks (59.1%) are much more than the sinistral ones (18.2%). In this subpart, there are 5 normal and no dextral fault-like cracks (Figure 12f).

Finally, another subdivision was carried out by splitting the 15-km long east 2 subpart into two 7.5-km long sub-subparts: east 2-1 to the "west" and east 2-2 to the "east" (Figure 12b). The median longitude (−73.410255°) of the subpart east 2 has been used to locate the separation line. East 2-1 contains 11 fault-like cracks of which 3 are sinistral, 3 are thrust, and 5 are normal (Figure 12g). East 2-2 also contains 11 fault-like cracks, 1 of which is sinistral and 10 are thrust (Figure 12h). The different subdivisions show that, in terms of percentage, thrust faults increase relative to sinistral fault-like cracks with progression to the east.

Furthermore, the overall contrast between the eastern and western parts seems to be present in crack magnitude. While about 60% of the cracks are located to the west (Figure 2b), the widest ones occur in this western part (Figure 13a). Indeed, to the east, crack openings are at most 20 cm; to the west, cracks are up to 30 cm. The same observation has been made for crack lengths (Figure 13b). To the east, crack lengths are between 3 and 300 m with the exception of some cracks in the marl of L'Asile (e.g., Figure 5d) that reach 455-m long. To the west, the lengths are up to 600 m.

5. Discussion

5.1. Cracks Grouped Along the Surface Trace of the Enriquillo Fault

The cracks are preferentially located along the Enriquillo fault zone. As a main shear zone creates surface complexities (Hobbs et al., 1976), the cracks may have used those zones of weakness during the earthquake. Different factors exacerbate that weakness. The area is a rainy region and particularly rainy during the year 2021 (Figure 4). In the case where some of the cracks had been generated during the post-seismic period, Hurricane Grace, which occurred 2 days after the mainshock, might have played an important role.

We showed that cracks were located in areas with high slope gradients, indicating susceptibility to slope breaks. However, the areas of high slope gradients are not random. They mainly correspond to different talus, riverbanks as well as fault scarps (e.g., Figures 5c, 6d, 9, and 10); these are all geomorphic features that are prone to instability in case of ground acceleration (Cabas et al., 2023).

Along the EPGF, the cracks also encounter about 60% of soft sediments of Quaternary alluvial sediments or continental Middle Miocene marls that are prone to failure. The Quaternary alluvial sediments come from numerous rivers along the fault zone. The latter controls the course of many rivers and the incision of many of those rivers may be facilitated by the fault activity. Thus, the crack occurrence was due to the interaction of different factors. Those factors can all be encountered along the Enriquillo fault zone. However, the tectonics seem to have more control over the others as the crack behavior appears to follow the slip pattern of the 2021 Haiti earthquake.

5.2. Crack Size and Map of Surface Deformation

The cracks described here are minor and do not allow a conventional rupture map on satellite imagery as it is often the case for large continental strike-slip earthquakes (e.g., Klinger et al., 2005, 2018; Rockwell & Klinger, 2013; Tchalenko & Ambraseys, 1970). Indeed, crack openings are below the spatial resolution of the high-resolution remote sensing data (e.g., Pléiades) acquired after the earthquake. Even if the lengths can be hundreds of meters, mapping is complicated without significant lateral displacement in a tropical environment. Therefore, plotting crack locations on a map (e.g., Figure 2a) and analyzing their characteristics with respect to local morphotectonics was our best choice.

The lateral offsets of a few centimeters measured here (e.g., Figure 7f) are rare and are not comparable to the 2–3 m measured by seismological and geodetic methods (Calais et al., 2022; Maurer et al., 2022; Okuwaki & Fan, 2022; Yin et al., 2023). Those minor offsets and other cracks may be the surface expression of the left-lateral strike-slip deformation at depth. Moreover, the minor offsets are found along the Ravine du Sud fault and near the only area where the rupture has reached the surface along the northern edge of the Camp-Perrin basin (Figure 14a). This area coincides with high gradient and discontinuity in the InSAR data (Calais et al., 2022; Raimbault et al., 2023). This is consistent with the relative abundance and prominence of the cracks in the western part of the rupture.

5.3. Crack Orientation and Coseismic Slip of the 2021 Earthquake

The orientation of cracks is mainly similar to that of sinistral and thrust faults in Haiti. While for thrust-like cracks we considered orientation between 100° and 160°, one might consider a narrower but correct interval between 100° and 150°. Another example is in the case of normal fault-like cracks whose orientation interval is between 10° and 70°, consistent with some mapped normal faults in Haiti (Mercier de Lépinay et al., 2011; Pubellier et al., 2000). Intervals for normal faults in Haiti can be as narrow as 15°–45°. We tested those alternative intervals and found the same pattern: more thrust to the east. Finally, our classification is based on fault mapping using high resolution data (Mercier de Lépinay et al., 2011; Saint Fleur et al., 2019) and is consistent with the strain ellipse shown in Figure 1.

Like in crack size, the east-west contrast has been evidenced in the crack orientation. To the west, most of the cracks tend to strike as sinistral faults and some strike as thrust faults. To the east, the dominant fault-like cracks are thrust and the second strike category is sinistral. This pattern is compatible with the general consensus on the slip model of the 14 August 2021 earthquake. Indeed, the rupture would have started in reverse motion on the EPGF as a transpressive structure and continued westward in almost purely left-lateral strike-slip motion on the Ravine du Sud fault (e.g., Calais et al., 2022; Douilly et al., 2023; Raimbault et al., 2023). By dividing the eastern part two times, we got more thrust-like cracks in the easternmost part at each subdivision (Figures 12e–12h). This indicates the influence of the slip pattern that creates more thrust motion eastward or more left-lateral strike-slip motion westward (Figures 14b and 14c). This is comparable to our slip model of the 12 January 2010 M_w 7.0 earthquake (Saint Fleur et al., 2015). Indeed, the rupture started on the Lamentin thrust (Figure 1) at a depth near its connection with the EPGF. The reverse motion on the Lamentin thrust promoted dominant reverse slip on the EPGF near the contact between the two fault planes, whereas strike-slip motion became dominant to the west as the perturbation created by the Lamentin thrust faded at short range (Saint Fleur et al., 2015). Likewise, we cannot exclude a similar scenario for the 14 August 2021 earthquake (Figures 14b and 14c). This would align with the reverse mechanisms of the aftershocks around the eastern part of the rupture (Douilly et al., 2023; Paul et al., 2023) as well as with the numerous reverse faults similar to the Lamentin fault that have been mapped onshore and offshore all along the northern boundary of the southern Peninsula (Calais et al., 2023; Mercier de Lépinay et al., 2011; Saint Fleur et al., 2019).

6. Conclusions

Overall, the 14 August 2021 earthquake occurred in a region which geology, topography and hydroclimatic conditions were favorable to ground failure. As a result, numerous landslides, rockfalls among others have been recorded. The linear cracks documented here are small and are not accompanied by significant horizontal offsets,

10.1029/2023GC011255

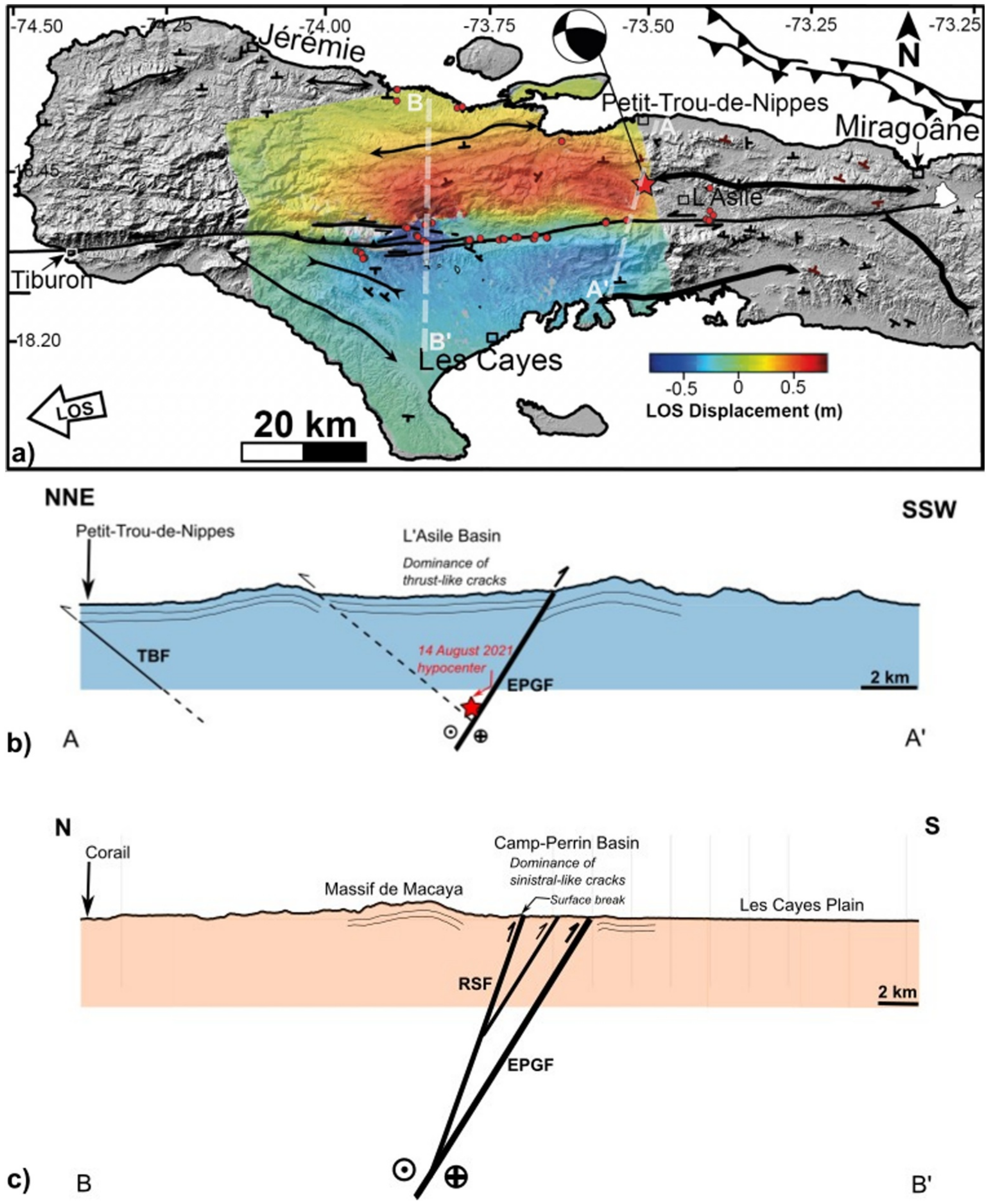

Figure 14. Crack location overlain on an interferogram from Raimbault et al. (2023) (ALOS-2 acquisitions along an ascending track on 23 December 2020 and 18 August 2021). Base map: ASTER hillshade image with geological information. White dotted lines locate cross-sections in (b) and (c) derived from ASTER Digital Elevation Model. (b) Interpretative cross-section through the eastern part of the 14 August 2021 rupture. The rupture could initiate on a 60°-north-dipping EPGF (Calais et al., 2022) or on a 40°-south-dipping thrust that triggered slip on the EPGF similar to the 12 January 2010 earthquake (Saint Fleur et al., 2015). This scenario as well as the location of the 2021 epicenter put constraints on the approximate location of the hypocenter (red star). TBF: Trois-Baies Fault; EPGF: Enriquillo-Plantain Garden Fault. (c) Interpretative cross-section through the western part of the rupture. Slip mainly occurred on the 71°-north-dipping Ravine du Sud Fault. Near that fault surface trace is 5-km long surface break observed on the InSAR data (Raimbault et al., 2023). For both cross-sections, the topographic profiles are provided with no vertical exaggeration; the depths are not at scale; depth colors mimic color code for eastern and western cracks in Figure 2.

as would be expected for an M_w 7.2 strike-slip event. As they are minor and influenced by many factors, the cracks generated during the 2021 earthquake might not be associated with primary fault surface breaks. However, their location is not random; they are preferentially located along the Enriquillo fault zone. As they are not primary fault surface ruptures, the cracks may use minor fault strands as areas of weakness. With crack strikes that are like thrust faults to the east and sinistral strike-slip faults to the west, the cracks present a similarity with the slip pattern during the earthquake. Despite the M_w 7.2 of the 2021 earthquake, no significant surface rupture was recorded, as was the case of 2010 M_w 7.0 earthquake. The two events are complex and involve thrust and strike-slip motion on at least two fault planes. As the coseismic deformation is distributed instead of being concentrated along a single fault plane, surface rupture may be rare for 2010-Haiti-like earthquakes. Finally, the 14 August 2021 earthquake is an interesting case at an oblique convergence margin. Despite the quasi absence of surface rupture, the cracks portray a partitioning into thrust and sinistral strike-slip that is compatible with the slip patten of the earthquake that is itself in accordance with the oblique convergence between the North American and Caribbean plates.

Data Availability Statement

The crack data presented here are available in Supporting Information S1 and archived at Saint Fleur, Dessable, et al. (2023). For data visualization, matplotlib (https://matplotlib.org/) and seaborn (https://seaborn.pydata.org/) have been mainly used. LiDAR data are from HaitiData & The World Bank (2021), available under the DOI https://doi.org/10.5069/G9GX48R8 and distributed by OpenTopogray (https://opentopography.org/). The SHIRPS data are detailed in Funk et al. (2014, 2015) and are available at https://data.chc.ucsb.edu/products/CHIRPS-2.0/.

Acknowledgments
This study was funded by the FEDER European Community program within Interreg Caraïbes through the "PREST" project and the CARIBACT joint research laboratory funded by IRD. It also partially benefits financial support from the IGCP/UNESCO project 693. Eric Calais acknowledges support from the Institut Universitaire de France and from the French National Research Agency (Project ANR-21CE03-0010 "OSMOSE"). We are grateful to the Centre National de l'Information Géo-Spatiale and Philémon Mondésir for providing the slope classes in Supporting Information S1. We thank Pete Peterson and Christian Emmanuel for useful discussions on the rainfall data. We thank URGéo staff and the Bureau des Mines et de l'Energie for their assistance in the field. Bryn Benford and an anonymous reviewer provided with constructive comments to improve the quality of the paper.

References

Bakun, W. H., Flores, C. H., & ten Brink, U. S. (2012). Significant Earthquakes on the Enriquillo Fault system, Hispaniola, 1500–2010: Implications for seismic hazard. *Bulletin of the Seismological Society of America*, *102*(1), 18–30. https://doi.org/10.1785/0120110077

Benford, B., DeMets, C., & Calais, E. (2012). GPS estimates of microplate motions, northern Caribbean: Evidence for a Hispaniola microplate and implications for earthquake hazard: *Microplate motions in the northern Caribbean*. *Geophysical Journal International*, *191*(2), 481–490. https://doi.org/10.1111/j.1365-246X.2012.05662.x

Benjamin, E., Bassily-Marcus, A. M., Babu, E., Silver, L., & Martin, M. L. (2011). Principles and practice of disaster relief: Lessons from Haiti. *Mount Sinai Journal of Medicine: A Journal of Translational and Personalized Medicine*, *78*(3), 306–318. https://doi.org/10.1002/msj.20251

Bien-aimé Momplaisir, R. (1986). *Contribution à l'étude géologique de la partie orientale du Massif de la Hotte (Presqu'île du Sud d'Haïti): Synthèse structurale des marges de la presqu'île à partir de données sismiques*. Université Pierre et Marie Curie (Paris VI).

Cabas, A., Lorenzo-Velazquez, C., Ingabire Abayo, N., Ji, C., Ramirez, J., Garcia, F. E., et al. (2023). Intersectional impacts of the 2021 Mw 7.2 Nippes, Haiti, earthquake from Geotechnical and social perspectives. *Bulletin of the Seismological Society of America*, *113*(1), 73–98. https://doi.org/10.1785/0120220118

Calais, É., Symithe, S., Mercier de Lépinay, B., & Prépetit, C. (2016). Plate boundary segmentation in the northeastern Caribbean from geodetic measurements and Neogene geological observations. *Comptes Rendus Geoscience*, *348*(1), 42–51. https://doi.org/10.1016/j.crte.2015.10.007

Calais, E., Symithe, S., Monfret, T., Delouis, B., Lomax, A., Courboulex, F., et al. (2022). Citizen seismology helps decipher the 2021 Haiti earthquake. *Science*, *376*(6590), 283–287. https://doi.org/10.1126/science.abn1045

Calais, E., Symithe, S. J., & de Lépinay, B. M. (2023). Strain partitioning within the Caribbean–north America Transform plate boundary in southern Haiti, tectonic and hazard implications. *Bulletin of the Seismological Society of America*, *113*(1), 131–142. https://doi.org/10.1785/0120220121

Darby, S. E., & Thorne, C. R. (1994). Prediction of tension crack location and riverbank erosion hazards along destabilized channels. *Earth Surface Processes and Landforms*, *19*(3), 233–245. https://doi.org/10.1002/esp.3290190304

Delorme, A., Grandin, R., Klinger, Y., Pierrot-Deseilligny, M., Feuillet, N., Jacques, E., et al. (2020). Complex deformation at shallow depth during the 30 October 2016 *M*w 6.5 Norcia earthquake: Interference between tectonic and gravity processes? *Tectonics*, *39*(2). https://doi.org/10.1029/2019TC005596

DeMets, C., Gordon, R. G., & Argus, D. F. (2010). Geologically current plate motions. *Geophysical Journal International*, *181*(1), 1–80. https://doi.org/10.1111/j.1365-246X.2009.04491.x

Douilly, R., Paul, S., Monfret, T., Deschamps, A., Ambrois, D., Symithe, S. J., et al. (2023). Rupture segmentation of the 14 August 2021 Mw 7.2 Nippes, Haiti, earthquake using aftershock relocation from a local seismic deployment. *Bulletin of the Seismological Society of America*, *113*(1), 58–72. https://doi.org/10.1785/0120220128

Funk, C., Peterson, P., Landsfeld, M., Pedreros, D., Verdin, J., Shukla, S., et al. (2015). The climate hazards infrared precipitation with stations—A new environmental record for monitoring extremes [Dataset]. *Scientific Data*, *2*(1), 150066. https://doi.org/10.1038/sdata.2015.66

Funk, C., Peterson, P. J., Landsfeld, M. F., Pedreros, D. H., Verdin, J. P., Rowland, J. D., et al. (2014). A quasi-global precipitation time series for drought monitoring (data series 832; data series, p. 4) [Dataset]. *USGS*. https://pubs.usgs.gov/ds/832/pdf/ds832.pdf

Giardina, G., Macchiarulo, V., Foroughnia, F., Jones, J. N., Whitworth, M. R. Z., Voelker, B., et al. (2023). Combining remote sensing techniques and field surveys for post-earthquake reconnaissance missions. *Bulletin of Earthquake Engineering*, *22*(7), 3415–3439. https://doi.org/10.1007/s10518-023-01716-9

Hackney, C. R., Darby, S. E., Parsons, D. R., Leyland, J., Best, J. L., Aalto, R., et al. (2020). River bank instability from unsustainable sand mining in the lower Mekong River. *Nature Sustainability*, *3*(3), 217–225. https://doi.org/10.1038/s41893-019-0455-3

HaitiData & The World Bank. (2021). Haiti digital terrain model 2014—2016 [Dataset]. https://doi.org/10.5069/G9GX48R8

Harris, C. R., Millman, K. J., Van Der Walt, S. J., Gommers, R., Virtanen, P., Cournapeau, D., et al. (2020). Array programming with NumPy. *Nature*, *585*(7825), 357–362. https://doi.org/10.1038/s41586-020-2649-2

Havenith, H.-B., Guerrier, K., Schlögel, R., Braun, A., Ulysse, S., Mreyen, A.-S., et al. (2022). Earthquake-induced landslides in Haiti: Analysis of seismotectonic and possible climatic influences. *Natural Hazards and Earth System Sciences*, *22*(10), 3361–3384. https://doi.org/10.5194/nhess-22-3361-2022

Hobbs, B. E., Means, W. D., & Williams, P. F. (1976). *An outline of structural geology*. Wiley.

Klinger, Y., Okubo, K., Vallage, A., Champenois, J., Delorme, A., Rougier, E., et al. (2018). Earthquake damage patterns resolve complex rupture processes. *Geophysical Research Letters*, *45*(19). https://doi.org/10.1029/2018GL078842

Klinger, Y., Xu, X., Tapponnier, P., Van der Woerd, J., Lassere, C., & King, G. (2005). High-resolution satellite imagery mapping of the surface rupture and slip distribution of the Mw 7.8, 14 November 2001 Kokoxili earthquake, Kunlun fault, northern Tibet, China. *Bulletin of the Seismological Society of America*, *95*(5), 1970–1987. https://doi.org/10.1785/0120040233

Lindsay, J. B. (2014). The Whitebox Geospatial analysis tools project and open-access GIS. In *Proceedings of the GIS research UK 22nd annual conference, the University of Glasgow*. https://doi.org/10.13140/RG.2.1.1010.8962

Mann, P., Calais, E., Ruegg, J.-C., DeMets, C., Jansma, P. E., & Mattioli, G. S. (2002). Oblique collision in the northeastern Caribbean from GPS measurements and geological observations: Oblique COLLISION in the northeastern Caribbean. *Tectonics*, *21*(6), 7-1–7-26. https://doi.org/10.1029/2001TC001304

Martin, S. S., & Hough, S. E. (2022). The 8 April 1860 Jour de Pâques Earthquake Sequence in Southern Haiti. *Bulletin of the Seismological Society of America*, *112*(5), 2468–2486. https://doi.org/10.1785/0120220016

Maurer, J., Dutta, R., Vernon, A., & Vajedian, S. (2022). Complex rupture and triggered aseismic creep during the 14 August 2021 Haiti earthquake from satellite geodesy. *Geophysical Research Letters*, *49*(11), 591. https://doi.org/10.1029/2022GL098573

Mercier de Lépinay, B., Deschamps, A., Klingelhoefer, F., Mazabraud, Y., Delouis, B., Clouard, V., et al. (2011). The 2010 Haiti earthquake: A complex fault pattern constrained by seismologic and tectonic observations: The 2010 Haiti earthquake fault pattern. *Geophysical Research Letters*, *38*(22), L22305. https://doi.org/10.1029/2011GL049799

Mohammed-Ali, W. S. (2020). Minimizing the detrimental effects of hydro-peaking on riverbank instability: The lower Osage river case—ProQuest [PhD, Missouri University of Science and Technology]. Retrieved from https://www.proquest.com/openview/25d22692d2f2e21413cf9e3f2acca745/1?pq-origsite=gscholar&cbl=18750&diss=y

Momplaisir, R., & Boisson, D. (1988). Carte Géologique de la République d'Haiti, South-West sheet (Les Cayes) (BME) [Carte]. Retrieved from http://bme.gouv.ht/carte/Feuille%20SW.jpg

Moreau de Saint-Méry, L.-É. (1798). Description topographique, physique, civile, politique et historique de la partie française de l'isle Saint-Domingue.

Okuwaki, R., & Fan, W. (2022). Oblique convergence Causes both thrust and strike-slip ruptures during the 2021 M 7.2 Haiti earthquake. *Geophysical Research Letters*, *49*(2), e2021GL096373. https://doi.org/10.1029/2021GL096373

Paul, S., Monfret, T., Courboulex, F., Delouis, B., Deschamps, A., Douilly, R., et al. (2023). The Miragoâne seismic clusters in southern Haiti triggered by the Mw 7.2 Nippes earthquake of August 14, 202. https://doi.org/10.5194/egusphere-egu23-13526

Pedregosa, F., Varoquaux, G., Gramfort, A., Michel, V., Thirion, B., Grisel, O., et al. (2011). Scikit-learn: Machine learning in Python. *Machine Learning in Python*, *12*, 2825–2830.

Possee, D., Keir, D., Harmon, N., Rychert, C., Rolandone, F., Leroy, S., et al. (2019). The tectonics and active faulting of Haiti from seismicity and tomography. *Tectonics*, *38*(3), 1138–1155. https://doi.org/10.1029/2018TC005364

Pubellier, M., Mauffret, A., Leroy, S., Vila, J. M., & Amilcar, H. (2000). Plate boundary readjustment in oblique convergence: Example of the Neogene of Hispaniola, greater Antilles. *Tectonics*, *19*(4), 630–648. https://doi.org/10.1029/2000tc900007

Pubellier, M., Vila, J.-M., & Boisson, D. (1991). North Caribbean neotectonic events: The Trans-Haitian fault system. Tertiary record of an oblique transcurrent shear zone uplifted in Hispaniola. *Tectonophysics*, *194*(3), 217–236. https://doi.org/10.1016/0040-1951(91)90262-Q

Raimbault, B., Jolivet, R., Calais, E., Symithe, S., Fukushima, Y., & Dubernet, P. (2023). Rupture geometry and slip distribution of the Mw 7.2 Nippes earthquake, Haiti, from space geodetic data. *Geochemistry, Geophysics, Geosystems*, *24*(4), e2022GC010752. https://doi.org/10.1029/2022GC010752

Rockwell, T. K., & Klinger, Y. (2013). Surface rupture and slip distribution of the 1940 Imperial valley earthquake, Imperial fault, southern California: Implications for rupture segmentation and dynamics. *Bulletin of the Seismological Society of America*, *103*(2A), 629–640. https://doi.org/10.1785/0120120192

Rodriguez, J., Havskov, J., Sørensen, M. B., & Santos, L. F. (2018). Seismotectonics of south-west Dominican Republic using recent data. *Journal of Seismology*, *22*(4), 883–896. https://doi.org/10.1007/s10950-018-9738-9

Saint Fleur, N., Dessable, J., Saint-Preux, G., Calais, E., Boisson, D., & Klinger, Y. (2021). Surface rupture of the 14 August 2021 Haiti earthquake. 2021, S42C-02.

Saint Fleur, N., Dessable, J. E., Saint-Preux, G., Calais, E., Feuillet, N., Boisson, D., et al. (2023a). Geologic reconnaissance and crack data of the 2021, Mw7.2, Haiti earthquake [Dataset]. *Zenodo*. https://doi.org/10.5281/ZENODO.10937970

Saint Fleur, N., Feuillet, N., Grandin, R., Jacques, E., Weil-Accardo, J., & Klinger, Y. (2015). Seismotectonics of southern Haiti: A new faulting model for the 12 January 2010 M 7.0 earthquake. *Geophysical Research Letters*, *42*(23), 10273. https://doi.org/10.1002/2015GL065505

Saint Fleur, N., Feuillet, N., & Klinger, Y. (2019). Active tectonics along the Cul-de-Sac-Enriquillo plain and seismic hazard for Port-au-Prince, Haiti. *Tectonophysics*, *771*, 228235. https://doi.org/10.1016/j.tecto.2019.228235

Saint Fleur, N., Klinger, Y., Dessable, J. E., Saint-Preux, G., Feuillet, N., Boisson, D., et al. (2023). Active tectonics in southern Haiti and surface rupture of the 14 August 2021 earthquake [other]. *Oral*. https://doi.org/10.5194/egusphere-egu23-14568

Saint Fleur, N., Klinger, Y., & Feuillet, N. (2020). Detailed map, displacement, paleoseismology, and segmentation of the Enriquillo-Plantain Garden Fault in Haiti. *Tectonophysics*, *778*, 228368. https://doi.org/10.1016/j.tecto.2020.228368

Tchalenko, J. S., & Ambraseys, N. N. (1970). Structural analysis of the Dasht-e Bayaz (Iran) earthquake Fractures. *Geological Society of America Bulletin*, *81*(1), 41. https://doi.org/10.1130/0016-7606(1970)81[41:SAOTDB]2.0.CO;2

Thorne, C. R., & Abt, S. R. (1993). Analysis of riverbank instability due to toe scour and lateral erosion. *Earth Surface Processes and Landforms*, *18*(9), 835–843. https://doi.org/10.1002/esp.3290180908

Troyanskaya, O., Cantor, M., Sherlock, G., Brown, P., Hastie, T., Tibshirani, R., et al. (2001). Missing value estimation methods for DNA microarrays. *Bioinformatics*, *17*(6), 520–525. https://doi.org/10.1093/bioinformatics/17.6.520

Valkaniotis, S., Ganas, A., Papathanassiou, G., & Papanikolaou, M. (2014). Field observations of geological effects triggered by the January–February 2014 Cephalonia (Ionian sea, Greece) earthquakes. *Tectonophysics*, *630*, 150–157. https://doi.org/10.1016/j.tecto.2014.05.012

Vallage, A., Klinger, Y., Lacassin, R., Delorme, A., & Pierrot-Deseilligny, M. (2016). Geological structures control on earthquake ruptures: The Mw 7.7, 2013, Balochistan earthquake, Pakistan. *Geophysical Research Letters*, *43*(19), 10163. https://doi.org/10.1002/2016GL070418

Virtanen, P., Gommers, R., Oliphant, T. E., Haberland, M., Reddy, T., Cournapeau, D., et al. (2020). SciPy 1.0: Fundamental algorithms for scientific computing in Python. *Nature Methods*, *17*(3), 261–272. https://doi.org/10.1038/s41592-019-0686-2

Wen, G., Li, X., Zhao, Y., Zhang, Y., Xu, C., & Zheng, Y. (2023). Kinematic rupture process and its Implication of a thrust and strike-slip multi-fault during the 2021 Haiti earthquake. *Remote Sensing*, *15*(7), 1730. https://doi.org/10.3390/rs15071730

10.1029/2023GC011255

Whitworth, M. R. Z., Giardina, G., Penney, C., Di Sarno, L., Adams, K., Kijewski-Correa, T., et al. (2022). Lessons for remote post-earthquake reconnaissance from the 14 August 2021 Haiti earthquake. *Frontiers in Built Environment*, *8*, 873212. https://doi.org/10.3389/fbuil.2022.873212

Yin, H. Z., Xu, X., Haase, J. S., Douilly, R., Sandwell, D. T., & Mercier de Lepinay, B. (2023). Surface deformation surrounding the 2021 Mw 7.2 Haiti earthquake illuminated by InSAR observations. *Bulletin of the Seismological Society of America*, *113*(1), 41–57. https://doi.org/10.1785/0120220109